nature microbiology

Article

https://doi.org/10.1038/s41564-025-02205-2

Decreased cytoplasmic crowding via inhibition of ribosome biogenesis can trigger *Candida albicans* filamentous growth

Received: 17 November 2024

Accepted: 23 October 2025

Published online: 10 December 2025

Check for updates

Antonio Serrano[1,8], Charles Puerner[1,9,10], Louis Chevalier[1,10], Emily Plumb[1], Johannes Elferich[2,3], Stephen Diggs[2], Ludwig Roman Sinn[4], Nikolaus Grigorieff[2,3], Markus Ralser[4,5,6], Morgan Delarue[7], Martine Bassilana[1] & Robert Alan Arkowitz[1]

The human fungal pathogen *Candida albicans* undergoes a morphological transition from a budding yeast to a filamentous form, which is associated with pathogenesis. Various cues mediate this transition including intracellular reorganization. The cytoplasm is densely packed with proteins including large macromolecular complexes, such as ribosomes, and hence, molecular crowding can impact a range of cellular processes. However, the relationship between cytoplasmic molecular crowding and morphological growth states is unclear. Using a fluorescent microrheological probe and single particle tracking, we observed a striking decrease in molecular crowding during filamentous growth in *C. albicans*. On the basis of simulations, proteomics and structural data from in situ cryogenic electron microscopy, we show that the reduction in crowding is due to a decrease in ribosome concentration that results in part from an inhibition of ribosome biogenesis, combined with an increase in cytoplasmic volume, leading to a dilution of ribosomes. Filamentation was enhanced in a mutant defective in ribosome biogenesis, while translation was not affected, suggesting that inhibition of ribosome biogenesis is a trigger for *C. albicans* morphogenesis. Overall, we show that filamentous growth is associated with reduced cytoplasmic crowding via changes in ribosome concentration, suggesting that combination therapies in which ribosome biogenesis is also targeted may be advantageous.

Fungal pathogens live in complex and dynamic environments in which survival and dissemination are key for a successful infection. One strategy to promote survival and dissemination during infections is the ability to change shape, that is, morphogenesis, and a number of fungi undergo dramatic cell shape changes[1]. However, changes in cell size and shape impose challenges for optimal growth and function. A number of fungal pathogens transition from an oval, budding form to a filamentous form; a striking example is the human fungal pathogen *Candida albicans*, which is a major fungal threat to public health, causing nosocomial and persistent mucosal infections[2–4]. In *C. albicans*, this morphological transition is critical for tissue adherence, penetration and damage—all of which promote a successful infection and dissemination to distinct sites[5,6]. A plethora of cues can trigger filamentous growth in this fungal pathogen, and while many studies have investigated intracellular reorganization during such morphogenesis[7], we know relatively little with respect to the cytoplasm and how its physical

A full list of affiliations appears at the end of the paper. e-mail: Robert.Arkowitz@univ-cotedazur.fr

https://doi.org/10.1038/s41564-025-02205-2

properties, which are critical for a range of chemical reactions and macromolecular assembly, are modulated during morphogenesis. Cytoplasmic fluidity, and more specifically, diffusivity at the mesoscale (the scale of protein complexes and machines, in tens to hundreds of nanometres), is inversely proportional to macromolecular crowding and viscosity. Viscosity affects the dynamics at the size scale of individual proteins, that is, ~10-fold smaller than the mesoscale, whereas crowding affects most strongly mesoscale particles[8,9].

The cytosol is a densely packed, viscous and crowded environment with protein concentrations on the order of hundreds of milligrams per millilitre. As a result, molecular crowding and viscosity can affect a range of biological functions[8–11], including chemical reaction rates, protein complex formation and rates of cytoskeletal protein polymerization[12–16]. In contrast to macromolecular crowding, viscosity affects the mobility at the scale of individual proteins. In the budding yeast *Saccharomyces cerevisiae* and mammalian cells, the target of rapamycin complex (TORC) was shown to regulate ribosome concentration, and inhibition of TORC1 resulted in increased diffusion of genetically encoded multimeric nanoparticles (GEMs)[17]. More recently, cell cycle arrest mutants were shown to result in decreased macromolecular crowding in the cytoplasm, in part via ribosome downregulation[18,19]. Little is known about the relationship between molecular crowding in the cytoplasm and morphological growth states, for example, during morphogenesis in *C. albicans*, a transition essential for virulence.

Here we show that there is a dramatic decrease in molecular crowding during filamentous growth, which is mediated by a specific inhibition of ribosome biogenesis and subsequent dilution of this critical cytoplasmic crowder as a result of growth. We propose that ribosome levels are tuned to regulate crowding in distinct growth states in this fungal pathogen. Furthermore, our results highlight that despite growth that occurs during the yeast-to-hyphal transition, there is a substantial decrease in ribosome levels.

Results

Increase in cytoplasmic mesoscale fluidity in filamentous cells scales with length

To investigate the link between cytoplasmic diffusivity at the mesoscale and cell morphology in *C. albicans*, we used nanometre-scale particles as tracers whose movements were followed over time, to measure the local mechanical properties of the cytoplasm. With these passive microrheological probes[17], that is, 40-nm GEMs, we measured cytoplasmic dynamics both in budding and hyphal cells. We imaged *C. albicans* cells expressing this probe, every 30 ms to obtain a signal sufficient for single particle tracking. The mean track length was 10 frames, which corresponds to 300 ms of imaging. The effective diffusion coefficient, D_{eff}, which is inversely proportional to viscosity for Brownian motion, was determined from the first 90 ms of acquisition. Temporal projections of the GEM trajectories that were false coloured in representative budding cells and cells treated with fetal bovine serum (FBS) for 60 min, in which a filament is evident, are shown in Fig. 1a. Fixation reduced the GEM D_{eff} of cells by over tenfold (Extended Data Fig. 1a). The median D_{eff} in budding cells was ~0.1–0.15 $\mu m^2 s^{-1}$ (Fig. 1b and Extended Data Fig. 1b). This value was independent of the GEM expression level, with a similar D_{eff} observed with *TEF1* and *ADH1* promoter-driven expression (Extended Data Fig. 1b), and somewhat lower than that observed in *S. cerevisiae*[17]. Furthermore, analysis of GEM movement did not reveal any cytoplasmic streaming, consistent with the lack of septal pores in *C. albicans* hyphae.

After 1–2 h of incubation in serum, filaments formed with an average length of 12 µm (range, 2–22 µm). We observed an increase in GEM D_{eff} of ~2-fold in these filamentous cells, which corresponds to a substantial fluidization of the cytoplasm at the mesoscale (Fig. 1b,c). We examined whether cytoplasmic diffusivity scaled with filament length, which is directly proportional to cell volume. Figure 1d shows such a correlation between filament length and cytoplasmic diffusivity; when values were grouped in 2-µm filament length bins, we observed a strong positive correlation between D_{eff} and filament length, with a Pearson coefficient of 0.93. Furthermore, there was also a small but

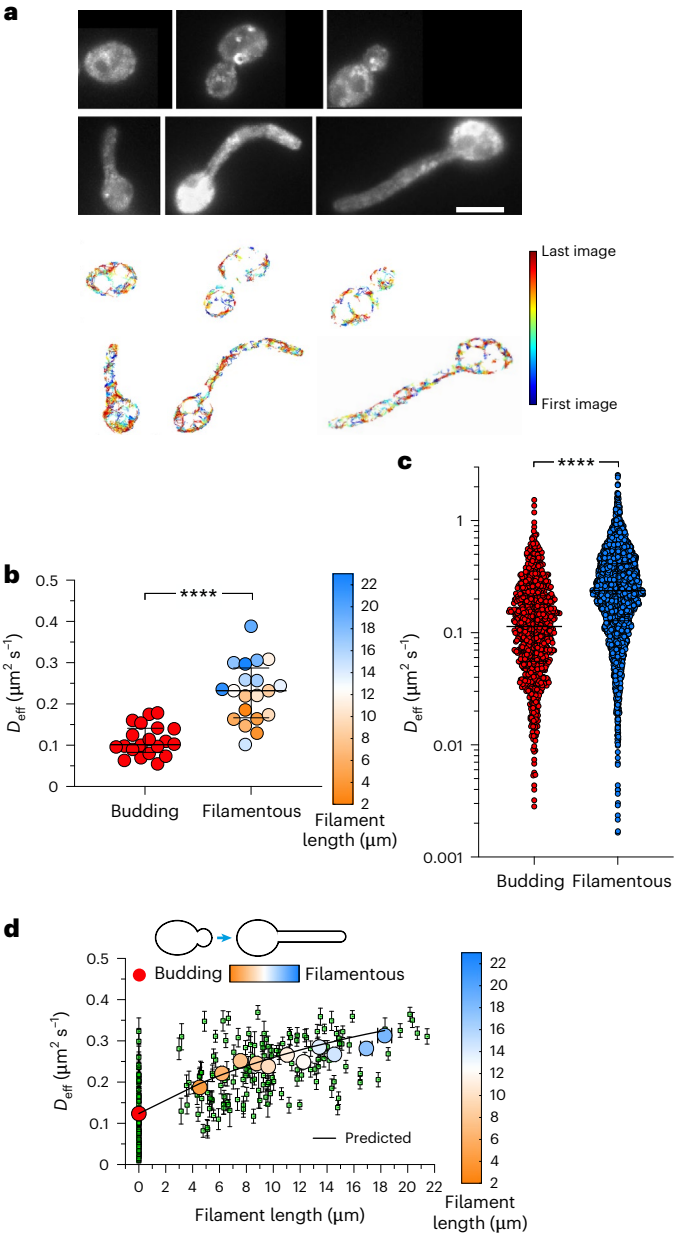

Fig. 1 | Cytoplasmic mesoscale fluidity increases with filament length. **a**, Projections of GEM trajectories. Representative budding and filamentous cells with maximum projection of GEM images (top) and particle trajectories of GEMs (bottom) are shown. False-coloured look up table is indicated. Scale bar, 5 µm. **b**, Substantial increase in GEM D_{eff} in filamentous cells. Filamentous growth was induced for 45–150 min. Each symbol is the median cell D_{eff} ($n = 20$ cells from 5 independent experiments; 10–350 trajectories per cell). Mean filament length, 12 µm; the colour gradient indicates length. Medians and interquartile ranges are indicated; $^{****}P < 0.0001$. **c**, Effective diffusion of all trajectories from budding and filamentous cells. Cells from **b**, with 900–3,300 trajectories for each condition. Medians and interquartile ranges are indicated; $^{****}P < 0.0001$. **d**, Cytoplasmic mesoscale fluidity increases with filament length. Filamentous growth was induced on agarose SC FBS, 45–125 min. The green squares are median cell D_{eff}, and the bars represent the s.e.m. Values are grouped in 2-µm filament length bins (red-to-blue gradient, with colours indicating lengths as above; $n = 10–26$ cells from three independent experiments; 1,700–2,600 trajectories). The red symbol indicates budding cells ($n = 67$; 2,500 trajectories). The solid black line is a fit using equation (2) using the overall cell volume; $r^2 = 0.95$.

https://doi.org/10.1038/s41564-025-02205-2

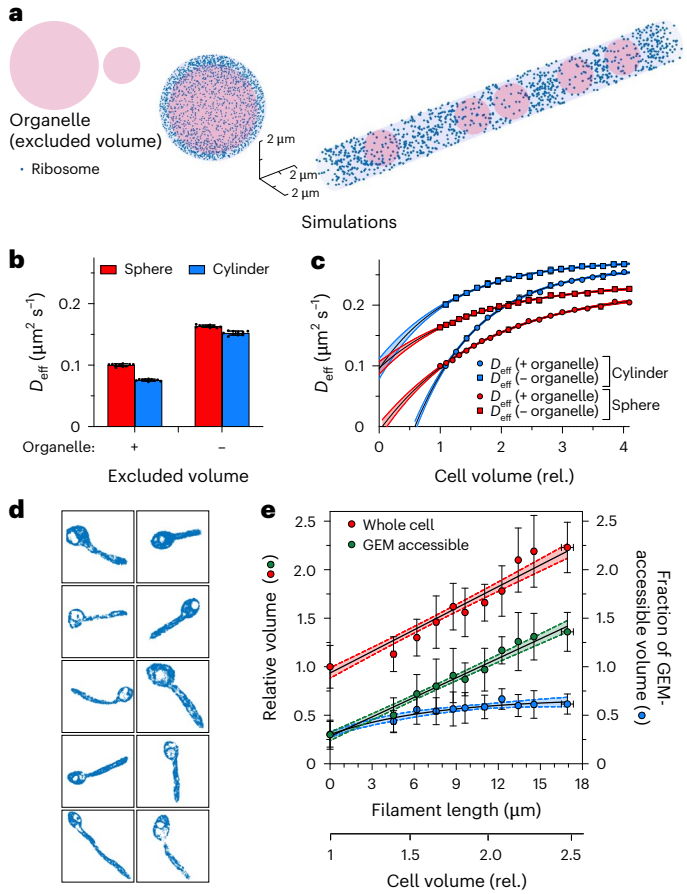

Fig. 2 | Simulations of GEM diffusion as a function of crowding and accessible volume. a, Representation of particle diffusion simulation with ribosomes (blue dots) and organelles (large pink spheres), within the cell boundaries. **b**, Effect of cell geometry and excluded internal volume on particle diffusion. Ribosome crowding was initially set to 20% of the cell volume, either in the presence or in the absence of an organellar compartment, which excluded an additional 60% of the cell. The bars indicate means from 10 simulations (symbols), with error bars indicating s.d. Note that the surface to volume ratio increases ~3-fold from a sphere to a cylinder of fungal cell size. **c**, Simulation of GEM diffusion upon cell volume increase. Particle D_{eff} in a cylindrical or spherical compartment (relative (rel.) volume), with ribosome crowders 20% at initial cell volume (square symbols). Simulations with excluded organelle compartments (for example, vacuoles; circle symbols) further reduced accessible volume from 80% (square symbols) to 20% (circle symbols). Values are D_{eff} means (6,000 particle simulations) carried out 10 times. Data fit with an exponential plateau equation, $r^2 > 0.99$, 95% confidence levels shown. **d**, Examples of GEM position over acquisition time highlight vacuoles in which GEMs are excluded. Representative cells in which GEM position is indicated by a circle of ~130 nm diameter equivalent. **e**, The GEM-accessible volume increases significantly as the filament extends. The positions of the GEMs and the outer edge of cells used in Fig. 1d were used to calculate the relative volume of the whole cell (red circle) and the GEM-accessible cytoplasm (green circle). The fraction of GEM-accessible volume (blue circle) is the volume of the GEM-accessible cytoplasm divided by the volume of the whole cell. Values are means with error bars indicating s.d.; data were fit either to a straight line (r^2 = 0.72–0.76) or to one phase association (r^2 = 0.48) for each condition with 95% confidence levels shown.

significant decrease in the median D_{eff} in the filament, compared with the mother compartment and whole cell (Extended Data Fig. 2a). This is consistent with changes in the surface area to volume, as shown in our diffusion simulations (Fig. 2a,b; compare the red sphere with the blue cylinder bars).

Mesoscale diffusivity scaling with increased cell volume suggests that during hyphal morphogenesis there is substantial dilution of a macromolecular crowder, such as ribosomes. To test this hypothesis, we simulated mesoscale particle diffusion in spherical and cylindrical cell geometries, using a simplified model that estimates diffusion based solely on Brownian motions and collisions with particles and crowders. An equivalent initial crowder per cell volume of 14,000 ribosomes per μm^3 cytosol was chosen, based on values from *S. cerevisiae*, which accounts for 20% of the initial cytosolic volume[17]. We also investigated the effect of the addition of large intracellular excluded volumes (analogous to vacuoles in volume, but any organelle, in principle) on the simulation of ribosome D_{eff} (Fig. 2). As expected, we found that in contrast to the small effects of cell geometry, the addition of inaccessible space reduced D_{eff} by 50–70%, depending on geometry. We anticipated that the increase in cytosolic volume in filamentous cells would be greater than that solely due to cell geometry changes, as for example, the vacuole, which is GEM inaccessible, has been shown to localize predominantly to the mother cell portion[20–22]. This was confirmed by visualizing all the GEM positions and trajectories (Fig. 2d and Extended Data Fig. 1c), as well as vacuoles specifically (Extended Data Fig. 3a–c), as an example organelle. Note that the GEM-inaccessible volume is greater than the vacuole volume, as it includes a range of additional organelles. Therefore, we simulated the effect of doubling the cell volume, which occurs approximately every hour during filament elongation, while maintaining constant the amount of cytoplasmic macromolecular crowder, which we initially assumed were ribosomes given their abundance and substantial cytosolic volume occupancy. Figure 2c shows that, in such a simulation (irrespective of geometry), we also observe an ~2-fold increase in D_{eff}, similar to the experimental data (Fig. 1d). These results are consistent with a significant dilution of a cytoplasmic macromolecular crowder due to both increased overall cell volume and accessible volume in the filament, as a result of less organelles such as vacuoles (Fig. 2e). Simulations revealed that this increase in D_{eff} was not substantially affected by the numbers of vacuoles and compartments, that is, fragmenting these compartments while maintaining their same overall volume, but was affected by the total surface area of crowders (Extended Data Fig. 3d). These simplified simulations are consistent with decreased cytoplasmic crowding from a combination of a constant number of ribosomes (for example, due to a decrease in ribosome biogenesis) and an increase in accessible volume.

Ribosome concentration decreases as hyphal filaments extend

On the basis of our simulations and a fit of our data using the simplified formalism that describes diffusion with respect to energy transfer in polydispersed mixtures (equation (2))[23], we estimated the concentration of ribosomes, assuming they were the main crowding agent. We assumed that during filament growth, ribosomes are only diluted (that is, no new synthesis). Fitting the experimental data using this equation allowed us to extract the initial concentration of ribosomes in the mother cell compartment, that is, 24,000 ± 300 ribosomes per μm^3 of cytosolic volume (Fig. 1d, predicted). In addition, when we took into account the fraction of GEM-accessible volume (Fig. 2e) in equation (2), we still observed a good fit to the experimental data, yielding a ribosome concentration (c_{ribo}) of 20,000 ± 700 μm^{-3} (Extended Data Fig. 3e), which is somewhat higher than that determined in *S. cerevisiae*[17]. The lower D_{eff} in *C. albicans* suggests that budding cells are more crowded in this fungal pathogen than in *S. cerevisiae*.

As ribosomes are likely to be a predominant cytoplasmic macromolecular crowder, we used liquid chromatography tandem mass spectrometry (LC–MS/MS) to determine the abundance of ribosomal proteins relative to the median cellular protein levels. Figure 3a shows that ribosomal protein levels decreased, relative to all other proteins, upon filamentation, compared with budding cells. This is in agreement with the decreased (~2-fold) levels of ribosomal RNA (rRNA) reported in *C. albicans* filamentous cells[24], as well as a substantial decrease in the transcripts of many ribosomal proteins upon filamentation[25]. To directly assess ribosome levels during morphogenesis, we carried

https://doi.org/10.1038/s41564-025-02205-2

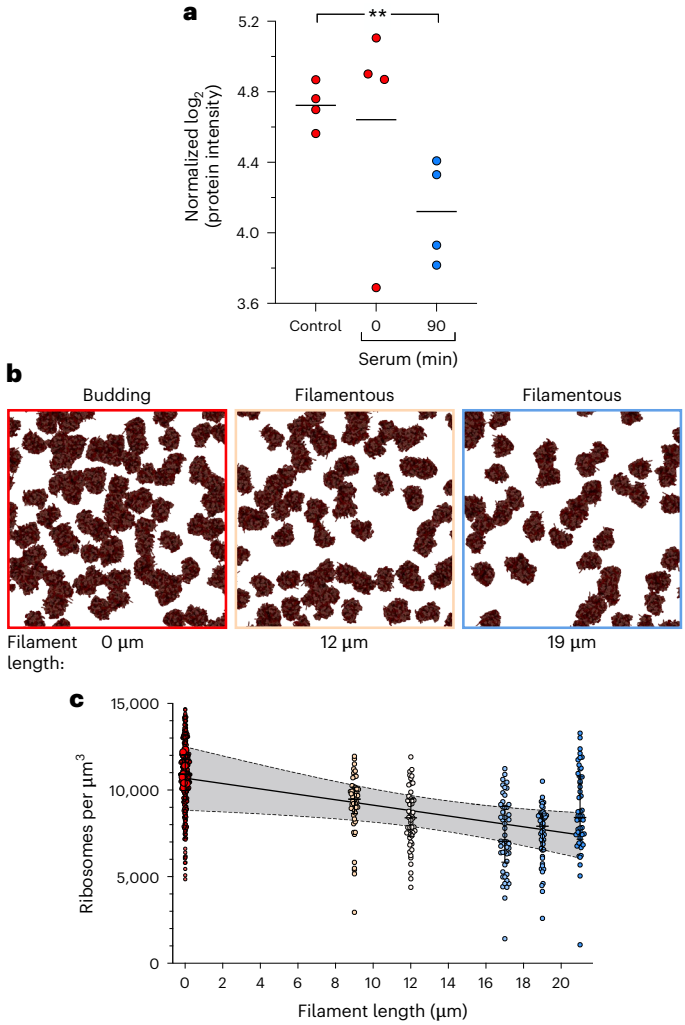

Fig. 3 | Ribosome concentration decreases with increasing filament length. **a**, Relative abundance of ribosomal proteins decreases upon filamentation. Ribosomal protein levels were determined by LC–MS/MS from independent ($n = 4$) replicates and normalized to the sample median protein levels. Control cells were grown in YEPD at 30 °C. In serum conditions, 50% FBS was added and samples were incubated at 37 °C for 0 and 90 min. Bars indicate means and unpaired t-test with $^{**}P < 0.01$. **b**, 60S ribosomal subunit density from representative ROI of cells in Extended Data Figs. 4 and 5 with filament lengths indicated. **c**, Ribosome density decreases with filament length. Ribosome concentration ($n = 8$ budding and 5 filamentous cells) was determined by cryo-EM 2DTM. Small symbols, values per ROI; large symbols, median of each budding cell (filament length, 0 µm). Medians and interquartile ranges are shown; symbol colours correspond to filament length. Fit of medians to a straight line, $r^2 = 0.77$ with 95% confidence levels shown; slope different from 0, $P < 0.0001$.

out cryogenic electron microscopy (cryo-EM) coupled with 2D template matching (2DTM) to identify 60S ribosomes[26,27] (Extended Data Figs. 4–7). Figure 3b shows that in filamentous cells there is a marked decrease in ribosome concentration, which is filament length dependent (Fig. 3c). Together, our results reveal that changes in crowding at the mesoscale occur, in part, via ribosomes, although we cannot exclude the possibility that there are also changes in cytosolic viscosity[16] and/or a decrease in the concentration of larger, slowly diffusing polysomes[28].

Cytosolic protein concentration and viscosity are similar in budding and filamentous cells

To address whether there was a decrease in cytosolic protein concentration and hence viscosity in filamentous cells, we analysed the concentration of the cytosolic fatty acid synthase (FAS) complex, as this 2.6-MDa barrel-shaped complex can be detected by cryo-EM. Figure 4a shows the reconstruction of the FAS complex detection in our cryo-EM images. Compared with the template derived from the cryo-EM structure of *C. albicans* FAS[29], our reconstruction shows density not present in the template and is also missing some density present in the template, consistent with true detections and not spurious correlations with noise[30]. Using 2DTM to identify FAS complexes, we did not observe a difference in the cytosolic FAS concentration between budding and filamentous cells (Fig. 4b). We next analysed the total cellular protein levels using fluorescein isothiocyanate (FITC)[31] to stain budding and filamentous cells, and Fig. 4c shows that the total protein concentration in these cells is similar, with only a 2% decrease in filamentous cells. Furthermore, the levels of cytosolic green fluorescent protein (GFP) in budding and filamentous cells were not statistically different (Fig. 4d). In response to changes in temperature, *S. cerevisiae* modulates cytosolic viscosity via regulation of glycogen and trehalose synthesis[16]. A comparison of glycogen levels in budding and filamentous cells showed no difference (Fig. 4e). Nonetheless, to confirm that the effects we observed were specific for the mesoscale and hence unlikely to be due to changes in viscosity, we also measured the mobility of GFP (~2 nm diameter) by fluorescence recovery after photobleaching (FRAP), as an indicator of GFP diffusion and cytosolic viscosity. Figure 4f shows that the average FRAP $t_{½}$ of GFP in budding and filamentous cells was 0.09 ± 0.01 (mean ± s.e.m.) at 37 °C (Fig. 4f), comparable to that determined in *S. cerevisiae*[16], indicating that cytosolic viscosity is similar in *C. albicans* budding and filamentous cells.

Furthermore, we analysed ribosomal states to determine whether there were differences between budding and filamentous cells (Extended Data Fig. 8a,b). In both cell types, the majority of ribosomes were in decoding states; there were no substantial differences between the ribosome states in budding and filamentous cells (Extended Data Fig. 8c). A fourfold reduction of polysome levels in *S. cerevisiae* during glucose deprivation resulted in a small (~10%) increase in GEM effective diffusion[32]. Hence, we analysed the clustering of ribosomes, as polysomes show a characteristic ribosome spacing[33], by first- and second-order point pattern, that is, a nearest neighbour function and Ripley's L function, respectively[34]. Extended Data Fig. 8d shows that the clustering of ribosomes is very similar in budding and hyphal cells, with distances between ribosomes ~28 nm, consistent with ribosome spacing in polysomes[35–37]. However as nearest neighbour analysis is sensitive to particle density, we also used Ripley's L function that determines spatial correlations between points at a range of distances[34]. Extended Data Fig. 8e shows that there was no decrease in ribosome clustering in filamentous cells, and at all indicated scales, there was increased clustering in ribosomes in filamentous cells compared with budding cells. Together our results suggest that the changes in mesoscale diffusivity are unlikely to be due to alterations in cytosolic viscosity or due to a substantial decrease in polysome levels.

Increased cytoplasmic mesoscale fluidity is not dependent on the actin cytoskeleton and cell growth

As osmotic stress alters macromolecular crowding, we examined how mesoscale cytoplasmic diffusivity was affected by changes in external osmolarity using sorbitol. At all sorbitol concentrations, we observed an increased GEM D_{eff} in filamentous compared with budding cells (Fig. 5a). Furthermore, a higher concentration of sorbitol is required to fully abolish GEM movement in filamentous cells, suggesting that molecular crowding in such cells is reduced (Extended Data Fig. 9a,b). We also examined whether mesoscale cytoplasmic diffusivity was affected by depolymerization of the actin cytoskeleton, as it was shown to decrease cytoplasmic diffusivity in *S. cerevisiae*[17], yet had no effect in *Schizosaccharomyces pombe*[38]. We used the marine toxin Latrunculin A (LatA) that prevents the polymerization of actin by binding and sequestering monomeric actin. Figure 5b and Extended Data Fig. 2c show that in budding *C. albicans* cells, the GEM D_{eff} increased ~35% following LatA disruption

https://doi.org/10.1038/s41564-025-02205-2

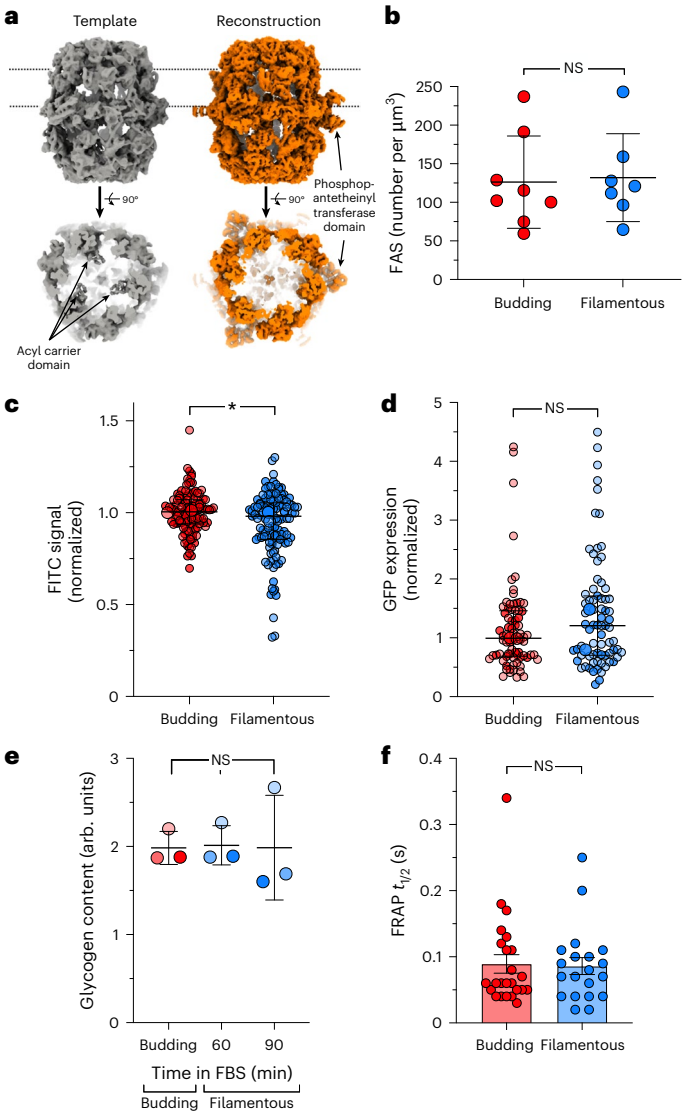

Fig. 4 | Cytosolic protein concentration is similar in budding and filamentous cells. a, Template and reconstruction of FAS. The template structure 6U5V[29] and reconstruction from 10,111 particles are shown. **b**, FAS concentration is similar between budding and filamentous cells. FAS concentration (n = 8 budding and 7 filamentous cells) was determined by cryo-EM 2DTM. Mean and s.d. are indicated; NS, not significant by two-sided unpaired t-test. **c**, Total protein concentration is similar in budding and filamentous cells. FITC was used to stain the total protein in budding and filamentous cells, and signals from sum projections of 24 × 0.3 µm z-section were quantitated. Values (n = 60 cells per experiment; small symbols, mean signals of individual cells; large symbols, medians of the experiment with interquartile ranges shown) were normalized to median budding signals for each experiment. *P < 0.05. **d**, GFP concentration is similar in budding and filamentous cells. GFP mean signals (n = 25–50 cells per experiment, 73 and 75 total cells from two independent experiments; small symbols, mean signals of individual cells (strain PY7398); large symbols, medians of the experiment with interquartile ranges indicated) normalized to median budding signals for each experiment. NS, not significant. Cells were imaged as in **c**. **e**, Glycogen levels are similar in budding and filamentous cells. Glycogen levels were determined enzymatically on the same number of budding and filamentous cells in three independent experiments each having three replicates; NS, not significant by unpaired t-test. **f**, The mobility of cytosolic GFP is similar in budding and filamentous cells. FRAP on indicated cells (strain PY7547, n = 20 and 24 cells from two independent experiments) at 37 °C, in the presence of serum for either 3–5 min (budding) or 60–90 min (filamentous). Mean and s.e.m. are indicated; NS, not significant.

of F-actin. By contrast, the same treatment had a substantially smaller effect on the GEM cytoplasmic dynamics in filamentous cells of similar lengths (Fig. 5c and Extended Data Fig. 2c). However, in LatA-treated filamentous cells, there was no longer a difference between the GEM D_{eff} in the filament compartment and that of the whole cell (Extended Data Fig. 2b), indicating that the actin cytoskeleton, rather than solely cell geometry, is important for the small difference in the cylindrical filaments (Fig. 2a,b). Overall, these results indicate that actin is more critical for cytoplasmic mesoscale crowding in budding cells compared with hyphal cells, in part due to the decreased accessible cytosolic volume in budding cells (Fig. 2e). As LatA also blocks growth, these

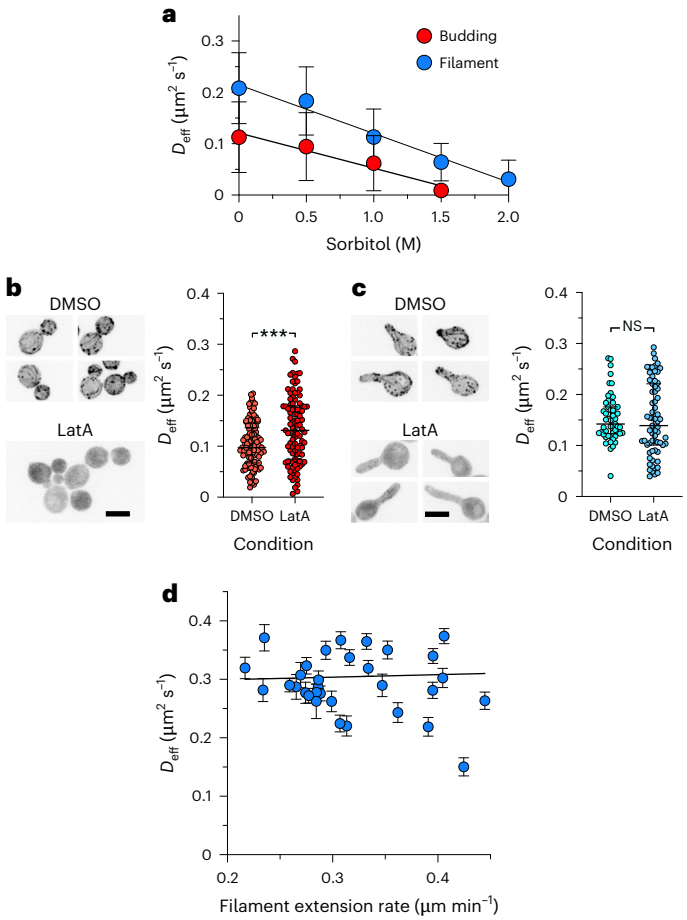

Fig. 5 | Cytoplasmic mesoscale fluidity is increased in filamentous cells irrespective of external osmolarity, and neither the actin cytoskeleton nor growth is critical for this increased fluidity. a, Cytoplasmic mesoscale fluidity is higher in filamentous cells, at different sorbitol concentrations. Symbols are the means of 20–95 cells from 4 independent experiments (11–200 trajectories per cell); bars denote s.d. Mean filament length was 7 ± 3 µm. **b**, Disruption of the actin cytoskeleton in budding cells increases cytoplasmic fluidity. Left: maximum projections of cells with LifeAct-RFP, with or without LatA. Right: symbols represent the median cell D_{eff} (n = 99 and 100 cells from 3 independent experiments; 10–180 trajectories per cell) with interquartile ranges shown; ***P = 0.0005. Scale bar, 5 µm. **c**, Disruption of the actin cytoskeleton in filamentous cells does not affect cytoplasmic fluidity. Left: maximum projections of cells induced for 45 min with or without LatA. Right: symbols represent the median cell D_{eff} (n = 51 and 67 cells from 3 independent experiments; 40–275 trajectories per cell) with interquartile ranges shown of filamentous cells with or without LatA; NS, not significant. Filament lengths ranged from 2.5 µm to 14 µm with an average of 7.6 ± 2.8 µm and 7.2 ± 3.4 µm, in cells treated with and without LatA, respectively. Scale bar, 5 µm. **d**, Cytoplasmic fluidity in filamentous cells is independent of growth rate. Cells were preincubated on agarose SC FBS for 40 min and monitored for 60 min (images were taken every 15–20 min). Each symbol represents the median cell D_{eff} with s.e.m. and cell extension rate (n = 32 cells from 2 independent experiments). The mean filament length was 17 ± 4 µm.

https://doi.org/10.1038/s41564-025-02205-2

results also reveal that growth per se does not substantially contribute to cytoplasmic mesoscale crowding in filamentous cells. This is further confirmed in Fig. 5d, which shows that over a twofold range of filament extension rates, GEM D_{eff} was essentially constant.

Inhibition of ribosome biogenesis results in increased cytoplasmic mesoscale fluidity and triggers filamentous growth

The increase in mesoscale diffusivity, as a result of the decreased ribosome concentration upon filament elongation, suggested that inhibition of ribosome biogenesis may be important for filamentous growth. To investigate the role of ribosome biogenesis in morphogenesis, we generated a mutant defective in the former process. *CGR1* encodes a protein that is critical for the processing of pre-rRNA in *S. cerevisiae*[39], in particular rRNA for the 60S ribosome subunit. Addition of doxycycline (Dox) to a *C. albicans* strain in which the sole copy of *CGR1* is under the control of the Tet-repressible promoter resulted in complete repression of the *CGR1* mRNA transcript (Fig. 6a) and in slow growth (Extended Data Fig. 9c). However, propidium iodide staining revealed that there was no difference in cell viability in the presence of Dox (1% inviable cells in the presence or absence of Dox, compared with 1% inviable in a control strain). Analyses of rRNA levels revealed a decrease in 28S and 18S rRNA upon *CGR1* repression (Fig. 6b) and a substantial (~1.7-fold) increase in GEM D_{eff} (Fig. 6c). Strikingly, repression of *CGR1* resulted in some filamentous cells in the absence of serum, which was not observed in the absence of Dox nor in wild-type cells (Fig. 6d). Furthermore, Fig. 6e shows a dramatic induction of hyphal-specific genes, for example, those encoding the G1 cyclin, *HGC1*; the candidalysin toxin, *ECE1*; and the hyphal cell wall glycoprotein, *HWP1*, in the *cgr1* mutant in the presence of Dox. We also examined whether hyphal-specific protein levels were increased using a reporter in which red fluorescent protein (RFP) was inserted behind the *HWP1* promoter. Figure 6f shows that RFP was expressed in essentially all filamentous cells (80%) induced upon *CRG1* repression. While it has been shown that inhibition of translation in *C. albicans* blocks the yeast-to-hyphal transition[40], we nonetheless examined whether repression of *CGR1* might alter translation and reduce protein levels. Total cellular protein levels were quantitated using FITC staining of budding cells in the absence of Dox and filamentous cells in the presence of Dox, and we did not detect a difference in cells in these two conditions (Extended Data Fig. 9d), indicating that overall translation was not substantially affected. The inhibition of the Tor kinase by rapamycin has been shown to reduce the number of ribosomes in *S. cerevisiae* and, similar to *CGR1* repression, resulted in hyphal-specific gene induction in *C. albicans*[41]. Together, these results reveal that inhibition of ribosomal biogenesis is important for the yeast-to-hyphal morphogenetic transition and that, upon filament elongation, dilution of ribosomes leads to a substantial reduction in cytoplasmic mesoscale crowding.

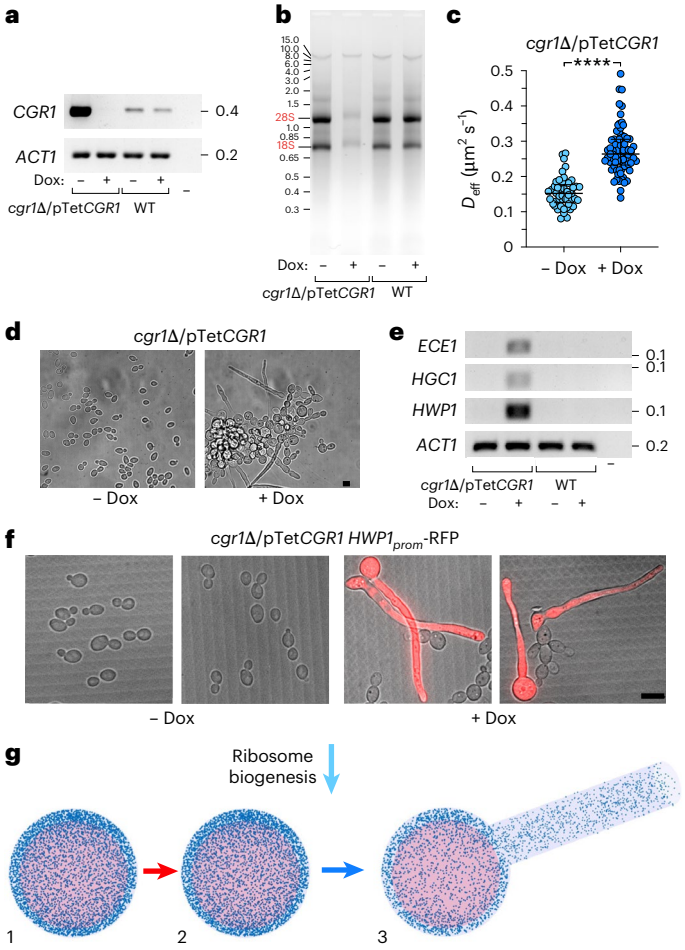

Fig. 6 | Inhibiting ribosome biogenesis increases cytoplasmic mesoscale fluidity and triggers filamentous growth. a, *CGR1* is fully repressed in doxycycline. The transcript level of *CGR1* was determined in *cgr1Δ*/pTet*CGR1* and wild-type strains, grown in the presence or absence of 5 μg ml^{-1} Dox by RT-PCR with *ACT1* used as an internal control (one experiment carried out). **b**, Repression of *CGR1* results in a decrease in rRNA. Total RNA was isolated from the indicated strains (three independent experiments carried out). **c**, *CGR1* repression increases cytoplasmic mesoscale fluidity. Each symbol represents the median cell D_{eff} (n = 49 and 75 cells from one experiment; 30–250 trajectories per cell), with medians and interquartile ranges indicated. Cells were grown with or without Dox, ****P < 0.0001. **d**, *CGR1* repression promotes filamentous growth. Representative cells with or without Dox (three independent experiments carried out). Scale bar, 5 μm. **e**, Hyphal-specific genes are induced upon *CGR1* repression. *ECE1*, *HGC1* and *HWP1* transcripts in indicated strains, with or without Dox; *ACT1* as internal control (one experiment carried out). **f**, Hyphal-specific protein levels are induced upon *CGR1* repression. Representative images of cells (strain PY7526) grown in the absence and presence of Dox. Images are composites of a differential interference contrast image and a maximum projection of 21 × 0.4 μm z-sections. No cells expressed *HWP1$_{prom}$*-RFP in the absence of Dox. The experiment was carried out three independent times. Scale bar, 5 μm. **g**, Schematic of ribosome biogenesis inhibition triggering morphogenesis. The red arrow indicates serum addition, which inhibits ribosome biogenesis (light blue arrow), leading to ribosome dilution upon growth (dark blue arrow). The blue dots are ribosomes and the pink spheres are organelle compartments inaccessible to ribosomes.

Discussion

Fungi can adopt a range of morphologies that are critical for interacting with their environment, in particular host cell damage and dissemination during an infection[1,5]. For example, *Ustilago maydis*, *Cryptococcus neoformans* and *C. albicans* can all switch between a budding and a filamentous form, and this morphological transition is important for virulence in these plant and human fungal pathogens[1,6,42]. These changes in cell shape and size impose constraints on biological function, in particular cytoskeletal organization, protein complex formation and chemical reaction rates that are critical for cell proliferation. The cytoplasm is a particularly crowded and complex milieu in which a substantial number of critical cellular biochemical reactions take place[8,9]. In this study, we took advantage of a genetically encoded microrheological probe[17] to investigate the cytoplasmic mesoscale diffusivity in *C. albicans* in budding and filamentous cells. Our results revealed how crowding in the cytoplasm changes during a dramatic morphological transition and indicate that the regulation of ribosome biogenesis is critical in triggering this transition.

Specifically, we show that crowding at the mesoscale is markedly reduced in hyphal filamentous cells and that this decrease in crowding is proportional to filament length. The substantial decrease in ribosome concentration in these cells, due to inhibition of ribosome biogenesis coupled with an increase in cytosolic volume, is likely to

contribute to the observed increase in mesoscale diffusivity. Analyses of the concentration of cytosolic proteins, including the FAS complex, total protein and cytosolic GFP, all indicate that ribosome levels are specifically reduced during filamentous growth, consistent with transcriptomic studies[25] and our mass spectrometry results. Interestingly, we do not observe significant differences in ribosome compositional and conformational states between budding and filamentous cells, and our analyses of ribosome clustering in these cells are consistent with polysome levels being similar, suggesting that the fraction of active ribosomes is similar in these two growth states.

Why would mesoscale crowding be reduced upon hyphal morphogenesis? While cytoplasmic streaming is thought to resolve the problems associated with slow diffusion in long filamentous cells[43], we have found no evidence of cytoplasmic streaming in *C. albicans* filaments, that is, the lack of directional bias in GEM trajectories. An attractive hypothesis is that increased mesoscale diffusivity in *C. albicans* filamentous cells is a means to partially overcome slow diffusion, particularly along the cell long axis. Consistent with this notion, our previous work revealed that the instantaneous velocities of secretory vesicles are increased in filamentous compared with budding cells[44]. Secretory vesicle and other organelle traffic, which is critical for filament extension, is likely to be sensitive to cytoplasmic crowding at the mesoscale. Furthermore, we speculate that decreased crowding at the mesoscale in filamentous cells favours protein translation, as modelling has indicated that molecular crowding limits translation and cell growth in bacteria[45]. Conversely, it has been shown in bacteria that inhibiting metabolic activity results in decreased cytoplasmic mesoscale diffusivity[46,47]. A recent computational model implicated ribosome–mRNA attachment and detachment in promoting mobility at the mesoscale[48], and while our analysis of ribosome compositional and conformational states, as well as clustering, does not reveal substantial differences between budding and filamentous cells, the dynamic nature of ribosome–polysome switching is likely to require approaches that probe such temporal dynamics. In *Escherichia coli*, a decrease in active ribosomes upon genome dilution and DNA replication arrest results in suboptimal growth[49]. It is intriguing that during filamentous growth there is a decrease in ribosome concentration while the proportion of active ribosomes is largely unaffected. Indeed in *S. cerevisiae*, a sizeable portion of ribosomes (at least 25%) do not contribute to translation[50]. In *C. albicans*, filamentous growth (0.3 μm min^{-1} extension) is similar with respect to volume increase, compared with budding growth (doubling every 90 min). In both *S. cerevisiae* and *S. pombe* cell cycle arrest mutants, which become enlarged, dilution of the cytoplasm, including ribosomes, is observed leading to increased cytoplasmic diffusion[18,19], which is distinct from the mesoscale-specific increase in diffusivity that we observe in *C. albicans* filamentous cells. Increased cytoplasmic fluidity can regulate cytoskeleton assembly and disassembly in vitro and in vivo[12,15,51], raising the possibility that decreased molecular crowding at the mesoscale could also be important for growth of long filamentous *C. albicans* cells. In summary, our results reveal that the dilution of ribosomes, subsequent to inhibition of their biogenesis, increases cytoplasmic diffusivity at the mesoscale during filamentous growth (Fig. 6g), and suggest that tuning ribosome numbers is critical for morphogenesis in this fungal pathogen.

Methods

Strains and media

Strains used in this study are listed in Supplementary Table 1a. For transformation, strains were grown in YEPD (yeast extract, peptone, dextrose) supplemented with uridine (80 μg ml^{-1}) at 30 °C. Cells were grown in YEPD medium, supplemented with uridine at 30 °C for budding growth. For filament induction cells, cells were either grown in YEPD liquid media with 50% FBS (PAN Biotech) or on agarose pads with 75% FBS in synthetic complete (SC) media, both at 37 °C. In all experiments that involved comparison with filamentous cells, budding cells were briefly incubated in the same media at 37 °C before imaging at the same temperature. For Dox gene repression, YEPD was supplemented with 5 μg ml^{-1} Dox. For sorbitol experiments, budding and filamentous cells were incubated with the indicated final concentrations of sorbitol for 5 min before imaging at 37 °C. For LatA actin depolymerizaton, cells were incubated with either 200 μM or 400 μM LatA, for budding and filamentous cells, respectively, for 15 min before imaging.

The oligonucleotides used in this study are listed in Supplementary Table 1b. The *PfV* gene, which encodes the subunits that comprise a 40-nm GEM[17], was codon optimized for *C. albicans* and synthesized (BaseClear). The *CaPfV* gene was cloned from the pUC57 vector into the pFA-GFPγ-URA3 plasmid using PstI sites, resulting in the pFA-CaPfV-GFPγ-URA3 plasmid. The *URA3* marker was replaced with either *CdHIS1* or *ARG4* markers, using unique AscI and PmeI restriction sites, resulting in pFA-CaPfV-GFPγ-CdHIS1 and pFA-CaPfV-GFPγ-ARG4. The GFPγ was then mutated using site-directed mutagenesis to a monomeric version using primers CaGFPγpA206K-BamHI/CaGFPγmA206K-BamHI, yielding pFA-CaPfV-GFPγ^{A206K}-CdHIS1 and pFA-CaPfV-GFPγ^{A206K}-ARG4. Subsequently these two plasmids were used as a template to PCR amplify the CaPfV-GFPγ^{A206K}-CdHIS1 and pFA-CaPfV-GFPγ^{A206K}-ARG4 cassettes for integration behind the endogenous *ADH1* promoter by using primers ADH1p-PfVp and CaADH1KIxFP_S2. The tetracycline repressible *cgr1*Δ/pTet*CGR1* strain was constructed from PY173, a derivative of BWP17 containing the tetracycline-regulatable transactivator TetR-ScHAP4AD, as described[52]. To visualize F-actin, a LifeAct reporter was used, which was derived from the plasmid pYGS974 (TEF1ΔLifeAct-GFP-HIS1/pJET)[53], in which GFP was replaced by mScarlet using primers NotITef1pLifeActS1 and CamScarletmAscI, resulting in pTEF1p-LifeAct-mScarlet-HIS1. This plasmid was digested with NotI/XbaI and integrated by homologous recombination in the *TEF1* locus. Strains expressing MLT1-GFPγ, ADH1p-GFPγ and HWP1p-mScarlet were constructed as described[54–56].

Microscopy, sample preparation and image analysis

Light microscopy. The GEM nanoparticles were imaged using Total Internal Reflection Fluorescence (TIRF) on a Nikon Ti eclipse inverted microscope (Nikon France S.A.S.) equipped with an iLas[2] scan head (Roper Scientific), an iXon 888 EMCCD camera (Andor Technology) and a ×100 CFI-APO-TIRF oil NA 1.49 objective. The laser illumination was with a 488-nm diode laser, with an intensity ranging between 10% and 60% and a TIRF angle of 56.24°. Images were acquired as a stream of 300–600 images in a single *Z* plane, with a 30-ms image acquisition and readout time, unless otherwise indicated. Temperature was controlled with an Okolab incubator at 37 °C, unless otherwise indicated. The LifeAct reporter was imaged using the spinning-disk confocal modality on the above-described microscope, equipped with a Yokogawa CSU-W1 (Yokogawa Electric), and using a 561-nm diode laser. Multi-positions were acquired with a motorized XYZ stage. The effective diffusion of the GEM particles was calculated as described[17], using the plugin Mosaic[57] in Fiji (version 1.54f) in a Windows 10/Intel computer and Matlab (version R2023a). Matlab was also used to generate the plots of all trajectories using a colormap and to split the filamentous cells to analyse the mother cell versus filament effective diffusion (scripts are available upon request). Extension rates were calculated as a function of filament length (measured with Fiji) per time.

Total cellular protein concentration was determined using FITC staining essentially as described[31]. Cells were fixed with 70% EtOH for 1 h; following washing, they were stained with 50 ng ml^{-1} FITC for 30 min and subsequently washed. Quantitation of total protein concentration using FITC labelling as well as cytosolic GFP concentration distribution was from sum projections, using the Matlab program HyphalPolarity[44]. Cell and vacuole volumes were extracted using a tailor-made Matlab program (described in detail elsewhere). After finding the object midplane, the program binarizes every z-section and fills in the identified vacuole or cell contour. Each identified pixel corresponds to a voxel,

and the total number of voxels represents the total volume. Volumes were extracted for each cell and compartments (mother and filament) were manually segmented. FRAP experiments were carried out as described[16] using a Zeiss LSM 980 confocal microscope with a ×63 NA 1.4 oil immersion objective with 30-mW diode 405-nm and 488-nm lasers. Images were acquired with a ×11 zoom resulting in a 191-nm pixel size, and images were separated by 27 ms. A circular bleach region of interest (ROI; 600 nm diameter) was used and data were analysed by easyFRAP, an open-source online FRAP analysis program[58]. Measurements with a mobile fraction <0.7 and single exponential curve fits with r^2 values < 0.4 were not analysed. The scale bar is 5 µm unless indicated otherwise.

Electron microscopy. Cryoplunging was carried out essentially as described[27]. Au grids (200 mesh) with a 2/2 silicone oxide support film were glow discharged on both sides for 45 s at 20 mA. Glycerol (5% final concentration) was added to the cells, and then immediately thereafter, 3 µl (0.2 OD_{600}) of cell suspension was applied to the support film side of the grids, blotted for 10 s and then frozen in liquid ethane using a cryoplunger (GP2 Leica). Focused ion beam (FIB) milling was carried out using an Aquilos 2 FIB–scanning electron microscope (SEM) (Thermo Fisher) with a stage cooled to less than −190 °C in a 35° AutoGrid sample holder. Grids were sputter coated with metallic Pt and then coated with organo-Pt essentially as described[27]. An overview of the grid was created by montaging SEM images, and isolated cells or cell clusters at the centre of grid squares were selected for FIB milling. Lamellae were generated automatically using the AutoTEM software (Thermo Fisher), with the following protocol: rough milling 1, 1 nA; medium milling 2, 0.3 nA (1.0° overtilt); fine milling, 0.1 nA (0.5° overtilt); finer milling, 0.1 nA (0.5° overtilt); and lamella polishing, 50 pA and 30 pA, 0.2° overtilt resulting in 150-nm-thick lamellae that were subsequently sputter coated with Pt for 5 s at a current of 5 mA.

FIB-milled grids were imaged in a Titan Krios TEM (Thermo Fisher) operated at 300 keV and equipped with a BioQuantum energy filter (Gatan) and K3 camera (Gatan). The instrument was controlled using SerialEM[59]. Individual lamellae were manually centred in the microscope and then moved to a position 60 µm below the eucentric height to achieve fringe-free illumination. The stage was tilted 15° to compensate for the milling angle, and overview images were obtained with a pixel size of 76.8 Å. Individual cells were annotated in these overview images using napari[60], and high-resolution montages were obtained for these cells using DeCo-LACE acquisition scripts[61]. The physical pixel size in high-resolution exposures was 1.05 Å, defocus was maintained at 1 µm and the total exposure was 30 e $Å^{-2}$. The exposures were dose fractionated into 30 frames.

Videos were imported into the *cis*TEM software package[62] and motion corrected using a custom version of unblur[63] as described[61], and binned to a final pixel size of 2.0 Å. Contrast transfer function parameters and sample thickness were estimated using CTFFIND5 (ref. 64). The structure of the vacant *C. albicans* 80S ribosome[65] (Protein Data Bank code: 7PZY) was modified by deleting subunits corresponding to the 40S subunit, and the resulting 60S structure was converted to a density map at 2.0 Å pixel size using the simulate program in *cis*TEM[66] using a B-factor scaling of 2. 2DTM of individual exposures was performed using the GPU-accelerated version of the match_template program in the *cis*TEM suite[26]. Rotation angles were searched using a 2 in-plane and 3 out-of-plane step size, and defocus values were searched within a 240-nm slab at a 40-nm step size. To quantify the abundance of FAS, we created a density map based on the structure of *C. albicans* FAS in the apo state[29] (Protein Data Bank code: 6U5V). Searches were performed identically to the 80S ribosomes, with the exception of accounting for the D3 symmetry. Image data and template matching results were montaged together as described[61].

The number of 60S ribosome subunits per imaged area was determined by manually segmenting cytosolic areas from the montaged cryo-EM images (Fig. 3b and Extended Data Figs. 4 and 5) and dividing the number of detections within the segmentation by the segmented area. The imaged volume was calculated by fitting the thickness of individual exposures, as estimated by CTFFIND5, to a two-dimensional cubic B-spline model with 3 knots[19] and integrating the estimated thickness at every pixel of the segmented area. The variation of this measurement was estimated by repeating this calculation in 50 random square areas with a side length of 200 nm within the segmented area.

To test for the collapse of polysomes, we performed two types of analysis. Firstly, we calculated the distance of each 60S detection to the closest 60S detection and plotted the resulting probability density function for the two conditions. Secondly, we calculated a Ripley's L metric in 20 shells ranging from 10 nm to 100 nm from the 3D coordinates of 60S detections using the RipleyK python package (https://github.com/SamPIngram/RipleyK). Boundary effects were corrected using a convex hull around the 60S detections. The L values were divided by the used radius, so that values smaller than 1 indicate dispersion and values larger than 1 indicate clustering.

To quantify the proportions of ribosomes in different states of translation, we extracted particle images around 60S detections. Particles from budding (n = 109,640) and filamentous cells (n = 57,017) were pooled into a single particle stack. Orientations and positions were refined by a single round of 'Manual Refinement' in *cis*TEM. The particle stack was binned to a pixel size of 8.0 Å, and particle parameters were exported into the Frealign format. Frealign (v 9.11_Aug2017)[67] was then used for classification of the particle stacks into 20 classes, without refinement of particle position or orientation, for 100 iterations. A spherical focus mask with a radius of 80 Å was placed over the A-site/GTPase (centre coordinates in Å: 216.7, 259.4, 347). The resulting 20 reconstructions were compared with states resulting from in situ single-particle analysis in *S. cerevisiae*[68] and, based on this, grouped into '60S', 'mRNA decoding', 'Peptidyl transfer' and 'tRNA translocation'. We then summed the mean occupancies of particles from budding or filamentous cells for all classes belonging to each group.

Modelling cytoplasmic diffusion

Predictive equations. A simplified formalism[23] was used to describe diffusion with respect to energy transfer in polydispersed mixtures to determine the fit to our experimental data, and from these equations (equations (1) and (2)), we derived the number of ribosome crowders:

$$D = D_0(1 - a\varphi);\ \varphi = \frac{V_{\mathrm{ribo}}}{V_{\mathrm{m}} + V_{\mathrm{f}}};\ a = \frac{(R_{\mathrm{ribo}} + R_{\mathrm{GEMs}})^2}{R_{\mathrm{GEMs}}^2} \quad (1)$$

With V_i being the volume of the ribosomes (ribo), the mother part of the cell (m) and the filament (f). D_0 is the diffusion coefficient of GEMs in the absence of ribosomes, but with other crowders in the cell. To avoid this unknown, we define $\widetilde{D_0}$ as the diffusion coefficient of GEMs when there is no filament (about 0.1 $\mu m^2\ s^{-1}$ in our case). This results in:

$$D = \widetilde{D_0}\frac{1 - \frac{V_{\mathrm{ribo}}a}{V_{\mathrm{m}}+V_{\mathrm{f}}}}{1 - \frac{V_{\mathrm{ribo}}a}{V_{\mathrm{m}}}} \quad (2)$$

We used equation (2) to fit our data. As we assume that no more ribosomes are produced during the growth of the filament, the total volume of ribosomes is fixed by the initial condition of the volume of the mother compartment, and is equal to $V_{\mathrm{ribo}} = c_{\mathrm{ribo}} \times \upsilon_{\mathrm{ribo}} \times V_{\mathrm{m}}$ where $\upsilon_{\mathrm{ribo}} = 4/3\pi {R_{\mathrm{ribo}}}^3$ is the volume of 1 ribosome, assuming a spherical geometry. The only unknown in equation (2) is thus c_{ribo}.

Simulations. A Matlab-based model (version R2023a) was developed to simulate particle diffusion within spherical and cylindrical boundaries, which we refer to as DiffSim. Particles of radii and concentration similar to those of ribosomes (r = 14 nm and 11,100 μm^{-3}) were randomly

localized within these geometries, together with larger spherical crowders (similar in size to a vacuole taking up 60% of the cell volume) that were immobile. To facilitate computation in this 3D simulation, cell geometries and excluded volumes were chosen accordingly. This highly simplified model accounts for the three main forces that influence particle diffusion: Brownian motion and collisions with both other particles and crowders. Brownian motion was modelled using a random walk algorithm, in which particles were displaced randomly at each time step. Collisions were simulated using a hard-sphere model, deflecting particles upon contact. Similarly, when particles encountered external boundaries, they were deflected back into the system. Particle positions were recorded in a matrix for subsequent analysis. The mean-squared displacement was calculated as a function of time (with Δt being identical to GEM acquisitions) to assess the D_{eff}, and its dependence on relative cell geometry and volume was determined. The D_{eff} was then determined from the slope of the mean-squared displacement curve using the Einstein–Smoluchowski equation, using the same sampling times as in the experimental acquisitions (90 ms). The accessible volume was determined using a custom Matlab program, which we refer to as AccessCyto, which analysed the positions of GEM particle tracks to calculate the region of the cell that was accessible to particle movement. The accessible volume was then compared with the total cell volume, by segmenting the maximum projections, to calculate the percentage of the cell accessible to the GEM particles. Scripts are available upon request.

Proteomics

Sample preparation was essentially as described[69]. Quality control samples to monitor LC–MS performance were created from pooling small aliquots of all samples. Peptide quantities were estimated via Quantitative Fluorometric Peptide Assay (Pierce). LC–MS-based proteomic data acquisition was performed as described[70]. In brief, samples were injected on an ACQUITY M-Class HPLC (Waters) connected to a ZenoTOF 7600 mass spectrometer with an Optiflow source (SCIEX), separated on an HSS T3 column (300 µm × 150 mm, 1.8 µm; Waters) using a 20-min active gradient. We used a Zeno SWATH acquisition scheme with 85 variable-sized windows and 11 ms accumulation time. LC–MS raw data were processed using DIA-NN 1.8 (ref. 71). First, a spectral library was predicted including the UniProt Proteome of *C. albicans* SC5314 (UP000000559), as well as the sequence of the GEM (see description above). For the main search, we enabled tryptic digestion allowing for one missed cleavage, no variable modification, N-terminal methionine excision and carbamidomethylation as fixed modification of cysteines. Mass accuracies were set to fall within 20 ppm and match-between-runs was enabled with protein inference on protein level. The obtained report was processed using Python 3.9 with the pandas (1.4.3) and NumPy (1.23.0) packages. Data were filtered to less than or equal to 1% FDR concerning Global.Q.Value, as well as PG.Q.Value and Lib.PG.Q.Value. Before the plotting, protein group quantities were sample-wise median normalized in two steps: first, subtracting the sample median in $\log_2$-space, then subtracting the $\log_2$-sample median of entities not belonging to the ribosome, according to UniProt annotated protein names (that is, containing '60S' or '40S', that is the 76 core ribosome proteins).

RNA extraction and RT-PCR

Cells were grown in YEPD media in the presence or absence of 5 µg ml^{-1} of Dox. RNA extraction and PCR with reverse transcription (RT-PCR) were carried out as described[72]. Oligonucleotide pairs ACT1.P1/ACT1.P2, CGR1.P1/CGR1.P2, ECE1.P1/ECE1.P2, HGC1.P1/HGC1.P2 and HWP1.P1/HWP1.P2 were used to amplify *ACT1*, *CGR1*, *ECE1*, *HGC1* and *HWP1*, respectively.

Statistical analysis

Data were compared by the Mann–Whitney two-sided *U* test unless otherwise indicated and where relevant and indicated the paired or unpaired *t*-test using GraphPad Prism (v. 8) software, with all *P* values indicated in the figure legends. Unless stated otherwise, medians and interquartile ranges are indicated. Pearson correlation coefficient and simple linear regression were determined using GraphPad Prism (v. 8) software.

Reporting summary

Further information on research design is available in the Nature Portfolio Reporting Summary linked to this article.

Data availability

All data supporting the findings of this study are available within the Article and Supplementary Information. The original micrographs of all cryo-EM data have been deposited in Electron Microscopy Public Image Archive (EMPIAR)[73] under accession code EMPIAR-12958. The density maps from the reconstructions of *C. albicans* FAS from cell slices using 2DTM, as well as ribosomes and its mRNA decoding, peptidyl transfer and tRNA translocation classes, have been deposited in Electron Microscopy Data Bank (EMDB)[74] (accession codes: EMD-72464, EMD-72486, EMD-72488, EMD-72489, EMD-72490), respectively. The mass spectrometry proteomics data have been deposited in the ProteomeXchange Consortium via the PRIDE[75] partner repository with the dataset identifier PXD067792. Source data are provided with this paper.

Code availability

Scripts are available upon request.

References

1. Min, K., Neiman, A. M. & Konopka, J. B. Fungal pathogens: shape-shifting invaders. *Trends Microbiol.* **28**, 922–933 (2020).
2. Lass-Florl, C. et al. Invasive candidiasis. *Nat. Rev. Dis. Primers* **10**, 20 (2024).
3. Schille, T. B., Sprague, J. L., Naglik, J. R., Brunke, S. & Hube, B. Commensalism and pathogenesis of *Candida albicans* at the mucosal interface. *Nat. Rev. Microbiol.* **23**, 525–540 (2025).
4. *WHO Fungal Priority Pathogens List to Guide Research, Development and Public Health Action* (World Health Organization, 2022).
5. Iliev, I. D. et al. Focus on fungi. *Cell* **187**, 5121–5127 (2024).
6. Katsipoulaki, M. et al. *Candida albicans* and *Candida glabrata*: global priority pathogens. *Microbiol. Mol. Biol. Rev.* **88**, e0002123 (2024).
7. Bassilana, M., Puerner, C. & Arkowitz, R. A. External signal-mediated polarized growth in fungi. *Curr. Opin. Cell Biol.* **62**, 150–158 (2020).
8. Holt, L. J. & Delarue, M. Macromolecular crowding: sensing without a sensor. *Curr. Opin. Cell Biol.* **85**, 102269 (2023).
9. Kim, H. & Delarue, M. Dynamic structure of the cytoplasm. *Curr. Opin. Cell Biol.* **94**, 102507 (2025).
10. Bonucci, M., Shu, T. & Holt, L. J. How it feels in a cell. *Trends Cell Biol.* **33**, 924–938 (2023).
11. Subramanya, A. R. & Boyd-Shiwarski, C. R. Molecular crowding: physiologic sensing and control. *Annu. Rev. Physiol.* **86**, 429–452 (2024).
12. Demosthene, B., Lee, M., Marracino, R. R., Heidings, J. B. & Kang, E. H. Molecular basis for actin polymerization kinetics modulated by solution crowding. *Biomolecules* https://doi.org/10.3390/biom13050786 (2023).
13. Kalinina, I. et al. Pivoting of microtubules around the spindle pole accelerates kinetochore capture. *Nat. Cell Biol.* **15**, 82–87 (2013).
14. Miermont, A. et al. Severe osmotic compression triggers a slowdown of intracellular signaling, which can be explained by molecular crowding. *Proc. Natl Acad. Sci. USA* **110**, 5725–5730 (2013).

15. Molines, A. T. et al. Physical properties of the cytoplasm modulate the rates of microtubule polymerization and depolymerization. *Dev. Cell* **57**, 466–479.e6 (2022).
16. Persson, L. B., Ambati, V. S. & Brandman, O. Cellular control of viscosity counters changes in temperature and energy availability. *Cell* **183**, 1572–1585.e16 (2020).
17. Delarue, M. et al. mTORC1 controls phase separation and the biophysical properties of the cytoplasm by tuning crowding. *Cell* **174**, 338–349.e20 (2018).
18. Tan, C., Lanz, M. C., Swaffer, M., Skotheim, J. & Chang, F. Intracellular diffusion in the cytoplasm increases with cell size in fission yeast. *Mol. Biol. Cell* https://doi.org/10.1091/mbc.E24-11-0488 (2025).
19. Terhorst, A. et al. The environmental stress response regulates ribosome content in cell cycle-arrested *S. cerevisiae*. *Front. Cell Dev. Biol.* **11**, 1118766 (2023).
20. Barelle, C. J. et al. Asynchronous cell cycle and asymmetric vacuolar inheritance in true hyphae of *Candida albicans*. *Eukaryot. Cell* **2**, 398–410 (2003).
21. Veses, V. & Gow, N. A. Vacuolar dynamics during the morphogenetic transition in *Candida albicans*. *FEMS Yeast Res.* **8**, 1339–1348 (2008).
22. Veses, V., Richards, A. & Gow, N. A. Vacuoles and fungal biology. *Curr. Opin. Microbiol.* **11**, 503–510 (2008).
23. Ilker, E., Castellana, M. & Joanny, J. F. Long-time diffusion and energy transfer in polydisperse mixtures of particles with different temperatures. *Phys. Rev. Res.* https://doi.org/10.1103/PhysRevResearch.3.023207 (2021).
24. Fleischmann, J. & Rocha, M. A. Decrease in ribosomal RNA in *Candida albicans* induced by serum exposure. *PLoS ONE* **10**, e0124430 (2015).
25. Nantel, A. et al. Transcription profiling of *Candida albicans* cells undergoing the yeast-to-hyphal transition. *Mol. Biol. Cell* **13**, 3452–3465 (2002).
26. Lucas, B. A. et al. Locating macromolecular assemblies in cells by 2D template matching with cisTEM. *eLife* https://doi.org/10.7554/eLife.68946 (2021).
27. Lucas, B. A., Zhang, K., Loerch, S. & Grigorieff, N. In situ single particle classification reveals distinct 60S maturation intermediates in cells. *eLife* https://doi.org/10.7554/eLife.79272 (2022).
28. Mohapatra, S. & Weisshaar, J. C. Functional mapping of the *E. coli* translational machinery using single-molecule tracking. *Mol. Microbiol.* **110**, 262–282 (2018).
29. Lou, J. W., Iyer, K. R., Hasan, S. M. N., Cowen, L. E. & Mazhab-Jafari, M. T. Electron cryomicroscopy observation of acyl carrier protein translocation in type I fungal fatty acid synthase. *Sci. Rep.* **9**, 12987 (2019).
30. Lucas, B. A., Himes, B. A. & Grigorieff, N. Baited reconstruction with 2D template matching for high-resolution structure determination in vitro and in vivo without template bias. *eLife* https://doi.org/10.7554/eLife.90486 (2023).
31. Knapp, B. D. et al. Decoupling of rates of protein synthesis from cell expansion leads to supergrowth. *Cell Syst.* **9**, 434–445.e6 (2019).
32. Xie, Y. et al. Polysome collapse and RNA condensation fluidize the cytoplasm. *Mol. Cell* **84**, 2698–2716.e9 (2024).
33. Ferguson, L. et al. Streamlined and sensitive mono- and di-ribosome profiling in yeast and human cells. *Nat. Methods* **20**, 1704–1715 (2023).
34. Martinez-Sanchez, A., Baumeister, W. & Lucic, V. Statistical spatial analysis for cryo-electron tomography. *Comput. Methods Programs Biomed.* **218**, 106693 (2022).
35. Arava, Y. et al. Genome-wide analysis of mRNA translation profiles in *Saccharomyces cerevisiae*. *Proc. Natl Acad. Sci. USA* **100**, 3889–3894 (2003).
36. Shah, P., Ding, Y., Niemczyk, M., Kudla, G. & Plotkin, J. B. Rate-limiting steps in yeast protein translation. *Cell* **153**, 1589–1601 (2013).
37. Warner, J. R. The economics of ribosome biosynthesis in yeast. *Trends Biochem. Sci.* **24**, 437–440 (1999).
38. Garner, R. M., Molines, A. T., Theriot, J. A. & Chang, F. Vast heterogeneity in cytoplasmic diffusion rates revealed by nanorheology and Doppelganger simulations. *Biophys. J.* **122**, 767–783 (2023).
39. Moy, T. I., Boettner, D., Rhodes, J. C., Silver, P. A. & Askew, D. S. Identification of a role for *Saccharomyces cerevisiae* Cgr1p in pre-rRNA processing and 60S ribosome subunit synthesis. *Microbiology* **148**, 1081–1090 (2002).
40. Oliver, G., de Ruiz Holgado, A. P. & Salim, R. Dimorphism in *Candida albicans*, effect of cycloheximide and acridine orange on germ-tube formation. *Mycopathologia* **79**, 43–47 (1982).
41. Bastidas, R. J., Heitman, J. & Cardenas, M. E. The protein kinase Tor1 regulates adhesin gene expression in *Candida albicans*. *PLoS Pathog.* **5**, e1000294 (2009).
42. Brown, G. D. et al. The pathobiology of human fungal infections. *Nat. Rev. Microbiol.* **22**, 687–704 (2024).
43. Goldstein, R. E. & van de Meent, J. W. A physical perspective on cytoplasmic streaming. *Interface Focus* **5**, 20150030 (2015).
44. Ghugtyal, V. et al. Phosphatidylinositol-4-phosphate-dependent membrane traffic is critical for fungal filamentous growth. *Proc. Natl Acad. Sci. USA* **112**, 8644–8649 (2015).
45. Klumpp, S., Scott, M., Pedersen, S. & Hwa, T. Molecular crowding limits translation and cell growth. *Proc. Natl Acad. Sci. USA* **110**, 16754–16759 (2013).
46. Jacobs-Wagner, C. Through the looking glass: an adventure into the metastable world of the bacterial cytoplasm. *Cell* **187**, 228–234 (2024).
47. Parry, B. R. et al. The bacterial cytoplasm has glass-like properties and is fluidized by metabolic activity. *Cell* **156**, 183–194 (2014).
48. Bera, P., Wasim, A., Bakshi, S. & Mondal, J. Protein translation can fluidize bacterial cytoplasm. *PNAS Nexus* **3**, pgae532 (2024).
49. Mäkelä, J. et al. Genome concentration limits cell growth and modulates proteome composition in *Escherichia coli*. *eLife* **13**, RP97465 (2024).
50. Metzl-Raz, E. et al. Principles of cellular resource allocation revealed by condition-dependent proteome profiling. *eLife* https://doi.org/10.7554/eLife.28034 (2017).
51. Chen, X., Roeters, S. J., Cavanna, F., Alvarado, J. & Baiz, C. R. Crowding alters F-actin secondary structure and hydration. *Commun. Biol.* **6**, 900 (2023).
52. Vernay, A., Schaub, S., Guillas, I., Bassilana, M. & Arkowitz, R. A. A steep phosphoinositide bis-phosphate gradient forms during fungal filamentous growth. *J. Cell Biol.* **198**, 711–730 (2012).
53. Zeng, G., Wang, Y. M. & Wang, Y. Cdc28-Cln3 phosphorylation of Sla1 regulates actin patch dynamics in different modes of fungal growth. *Mol. Biol. Cell* **23**, 3485–3497 (2012).
54. Garcia-Rodas, R. et al. Plasma membrane phosphatidylinositol-4-phosphate is not necessary for *Candida albicans* viability yet is key for cell wall integrity and systemic infection. *mBio* https://doi.org/10.1128/mbio.03873-21 (2022).
55. Puerner, C. et al. Mechanical force-induced morphology changes in a human fungal pathogen. *BMC Biol.* **18**, 122 (2020).
56. Puerner, C., Serrano, A., Wakade, R. S., Bassilana, M. & Arkowitz, R. A. A myosin light chain is critical for fungal growth robustness in *Candida albicans*. *mBio* **12**, e0252821 (2021).
57. Sbalzarini, I. F. & Koumoutsakos, P. Feature point tracking and trajectory analysis for video imaging in cell biology. *J. Struct. Biol.* **151**, 182–195 (2005).

58. Koulouras, G. et al. EasyFRAP-web: a web-based tool for the analysis of fluorescence recovery after photobleaching data. *Nucleic Acids Res.* **46**, W467–W472 (2018).
59. Mastronarde, D. N. Automated electron microscope tomography using robust prediction of specimen movements. *J. Struct. Biol.* **152**, 36–51 (2005).
60. Ahlers, J. et al. napari: a multi-dimensional image viewer for Python (v0.4.18). *Zenodo* https://doi.org/10.5281/zenodo.8115575 (2023).
61. Elferich, J., Schiroli, G., Scadden, D. T. & Grigorieff, N. Defocus Corrected Large Area Cryo-EM (DeCo-LACE) for label-free detection of molecules across entire cell sections. *eLife* https://doi.org/10.7554/eLife.80980 (2022).
62. Grant, T., Rohou, A. & Grigorieff, N. *cis*TEM, user-friendly software for single-particle image processing. *eLife* https://doi.org/10.7554/eLife.35383 (2018).
63. Grant, T. & Grigorieff, N. Measuring the optimal exposure for single particle cryo-EM using a 2.6 A reconstruction of rotavirus VP6. *eLife* **4**, e06980 (2015).
64. Elferich, J., Kong, L. & Grigorieff, N. CTFFIND5 provides improved insight into quality, tilt and thickness of TEM samples. *eLife* https://doi.org/10.7554/eLife.97227.1 (2024).
65. Zgadzay, Y. et al. E-site drug specificity of the human pathogen *Candida albicans* ribosome. *Sci. Adv.* **8**, eabn1062 (2022).
66. Himes, B. & Grigorieff, N. Cryo-TEM simulations of amorphous radiation-sensitive samples using multislice wave propagation. *IUCrJ* **8**, 943–953 (2021).
67. Grigorieff, N. Frealign: an exploratory tool for single-particle cryo-EM. *Methods Enzymol.* **579**, 191–226 (2016).
68. Cheng, J. et al. Capturing eukaryotic ribosome dynamics in situ at high resolution. *Nat. Struct. Mol. Biol.* **32**, 698–708 (2025).
69. Messner, C. B. et al. The proteomic landscape of genome-wide genetic perturbations. *Cell* **186**, 2018–2034.e21 (2023).
70. Wang, Z. et al. High-throughput proteomics of nanogram-scale samples with Zeno SWATH MS. *eLife* https://doi.org/10.7554/eLife.83947 (2022).
71. Demichev, V., Messner, C. B., Vernardis, S. I., Lilley, K. S. & Ralser, M. DIA-NN: neural networks and interference correction enable deep proteome coverage in high throughput. *Nat. Methods* **17**, 41–44 (2020).
72. Basante-Bedoya, M. A. et al. Two distinct lipid transporters together regulate invasive filamentous growth in the human fungal pathogen *Candida albicans*. *PLoS Genet.* **18**, e1010549 (2022).
73. Iudin, A. et al. EMPIAR: the Electron Microscopy Public Image Archive. *Nucleic Acids Res.* **51**, D1503–D1511 (2023).
74. The wwPDB Consortium. EMDB—the Electron Microscopy Data Bank. *Nucleic Acids Res.* **52**, D456–D465 (2024).
75. Perez-Riverol, Y. et al. The PRIDE database at 20 years: 2025 update. *Nucleic Acids Res.* **53**, D543–D553 (2025).

Acknowledgements

We thank P. Silva, H. Labbaoui and S. Bogliolo for assistance, S. Noselli and A. Hubstenberger for comments on the paper, the PRISM Imaging facility (B. Monterroso and S. Ben-Aicha) and the Microscopy Imaging Cytometry d'Azur (MICA) for microscopy support (the Zeiss LSM 980 was acquired with funds from Conseil départemental—Alpes-Maritimes CD06 and Inserm ITMO Cancer), the BIOINFO Bioinformatic facility (A. Fortuné) for computational support and M. Rigney for support with cryo-EM sample preparation. Cryo-EM data were acquired at the UMass Chan Medical School Cryo-EM Core Facility. This work was supported by the CNRS, INSERM, Université Côte d'Azur, ANR (ANR-19-CE13-0004-01, R.A.A.), EC (MSCA-ITN-2015-675407, R.A.A.; MSCA-IF-2020-101029870, A.S. and R.A.A.; ERC-SyG-2020 951475, R.A.A. and M.R.), the German Ministry of Education and Research (BMBF) MSCoreSys (031L0220, M.R.), FRM (FDT202404018460, E.P. and R.A.A., and SPF202309017657, L.C. and R.A.A.) and NIH (TL1TR001454, N.G.) grants.

Author contributions

R.A.A. conceptualized the project. Experimental and computational analyses were carried out by A.S., C.P., L.C., E.P., J.E., S.D., L.R.S., M.D. and R.A.A. The paper was written by M.B. and R.A.A. Mass spectrometry was carried out by L.R.S. and M.R., and cryo-EM by J.E., S.D. and N.G.

Competing interests

The authors declare no competing interests.

Additional information

Extended data is available for this paper at https://doi.org/10.1038/s41564-025-02205-2.

Supplementary information The online version contains supplementary material available at https://doi.org/10.1038/s41564-025-02205-2.

Correspondence and requests for materials should be addressed to Robert Alan Arkowitz.

Peer review information *Nature Microbiology* thanks Arnold Boersma, Sophie Martin and the other, anonymous, reviewer(s) for their contribution to the peer review of this work. Peer reviewer reports are available.

Reprints and permissions information is available at www.nature.com/reprints.

Publisher's note Springer Nature remains neutral with regard to jurisdictional claims in published maps and institutional affiliations.

[1]Université Côte d'Azur, CNRS, INSERM, Institute of Biology Valrose (iBV), Nice, France. [2]RNA Therapeutics Institute, University of Massachusetts Chan Medical School, Worcester, MA, USA. [3]Howard Hughes Medical Institute, University of Massachusetts Chan Medical School, Worcester, MA, USA. [4]Department of Biochemistry, Charité—Universitätsmedizin Berlin, Freie Universität Berlin and Humboldt-Universität zu Berlin, Berlin, Germany. [5]Berlin Institute of Health (BIH) at Charité—Universitätsmedizin Berlin, Berlin, Germany. [6]Max Planck Institute for Molecular Genetics, Berlin, Germany. [7]LAAS-CNRS, University of Toulouse, CNRS, Toulouse, France. [8]Present address: Centro de Biotecnología y Genómica de Plantas, Universidad Politécnica de Madrid (UPM)—Instituto Nacional de Investigación y Tecnología Agraria y Alimentaria (INIA/CSIC), Pozuelo de Alarcón, Spain. [9]Present address: Department of Microbiology and Immunology, Geisel School of Medicine at Dartmouth, Hanover, NH, USA. [10]These authors contributed equally: Charles Puerner, Louis Chevalier. ✉e-mail: Robert.Arkowitz@univ-cotedazur.fr

https://doi.org/10.1038/s41564-025-02205-2

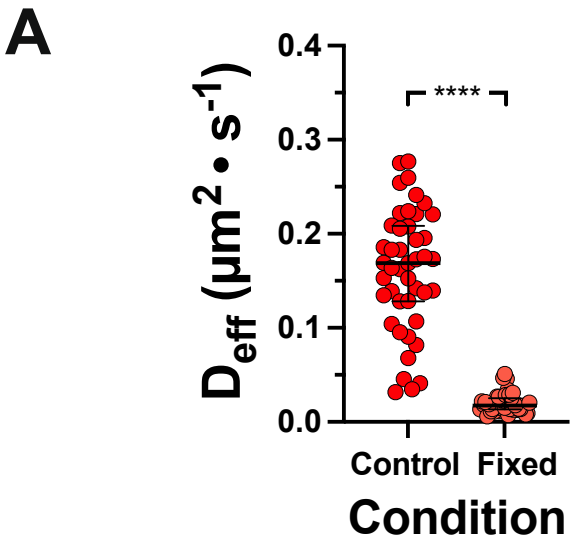

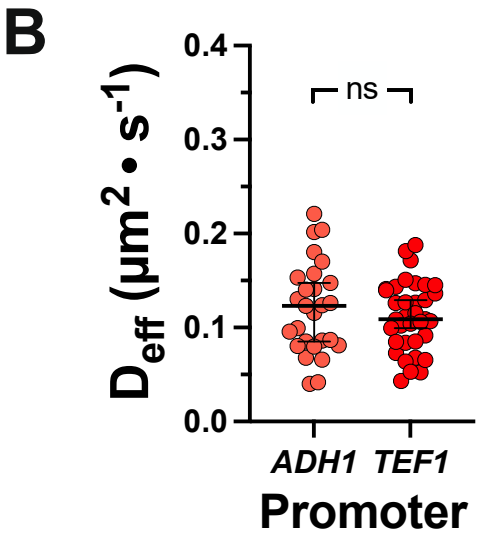

Extended Data Fig. 1 | GEMs are largely immobile in fixed cells and their mobility is independent of expression level. A) Each symbol represents the median D_{eff} of indicated cells (n = 42 and 44 cells from one experiment; 15-135 trajectories per cell), expressing GEMs under the control of the *TEF1* promoter, grown at 30 °C and fixed with para-formaldehyde, with medians and interquartile range indicated; **** < 0.0001. **B**) Each symbol represents the median D_{eff} of indicated cells (n = 27 and 35 cells from one experiment; 25-120 trajectories per cell), expressing GEMs under the control of either the *ADH1* or the *TEF1* promoter and grown at 30 °C, with medians and interquartile range indicated; ns not significant. **C**) Projections of GEM trajectories. Representative budding and filamentous cells with all GEM particle trajectories shown. Trajectories are false colored according to when during acquisition they were observed (see Fig. 1a).

https://doi.org/10.1038/s41564-025-02205-2

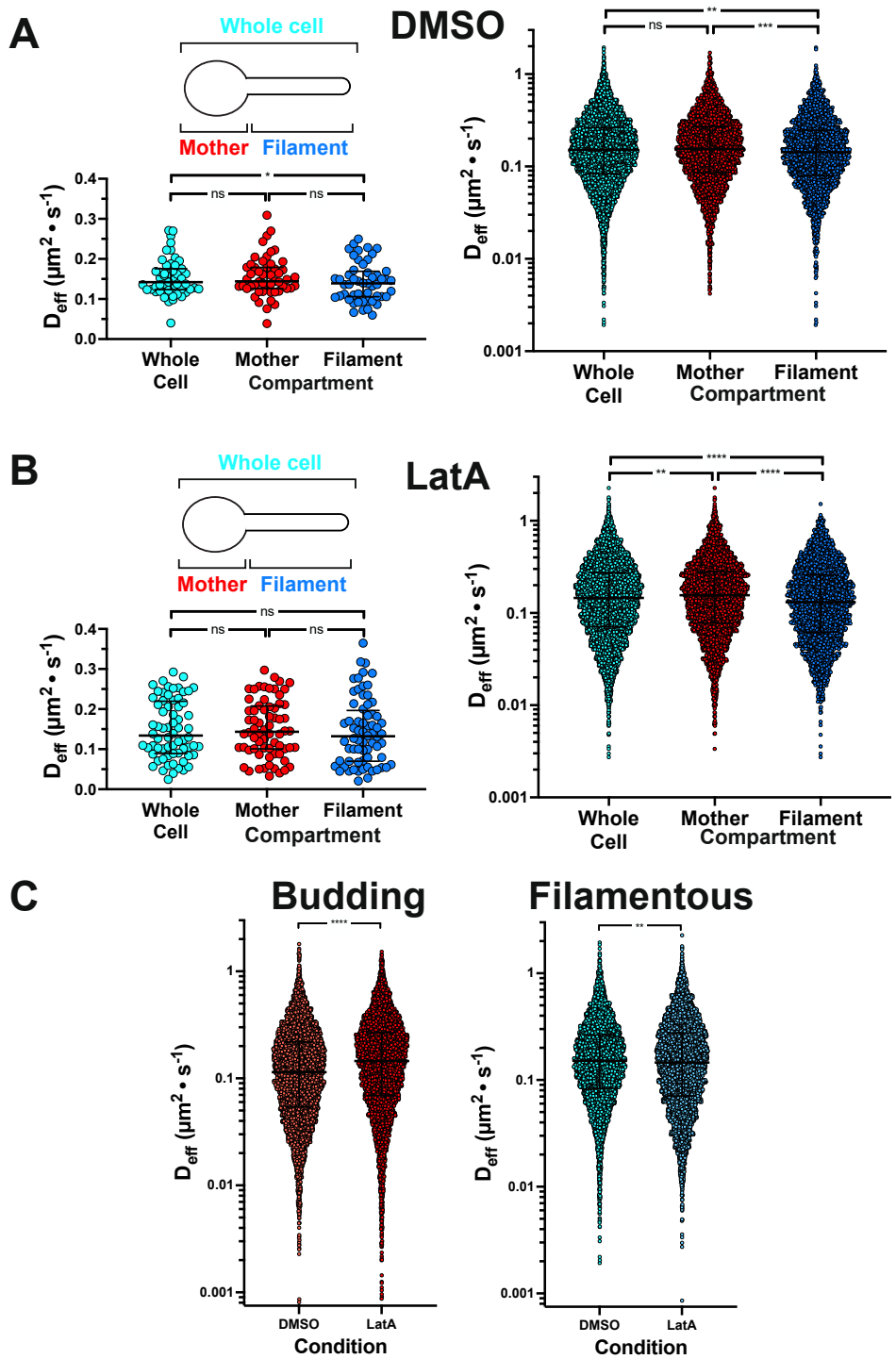

Extended Data Fig. 2 | GEM effective diffusion is somewhat reduced in filament compartment. A) GEM effective diffusion in filament and mother cell compartments. Left panel: median D_{eff} of cells (n = 51) from Fig. 5c (mean filament length 7 µm), in the absence of latrunculin A (LatA), with trajectories in whole cell, as well as mother and filament compartments analyzed. Medians and interquartile ranges are indicated, with * < 0.05 paired t-test. Right panel: effective diffusion of all trajectories from filamentous cells from Fig. 5c in the absence of LatA, with trajectories in whole cell (n = 7440), mother (n = 4525) and filament compartments (n = 2870) analyzed. Medians and interquartile ranges are indicated, with *** < 0.001, ** < 0.01 and ns not significant. **B**) GEM effective diffusion is similar in the mother and filament cell compartments upon disruption of the actin cytoskeleton. Left panel: median D_{eff} of cells (n = 67) from Fig. 5c in the presence of LatA (mean filament length 7 µm), with all trajectories in whole cell, mother and filament compartments analyzed. Medians and interquartile ranges are indicated with ns not significant paired t-test. Right panel: effective diffusion of all trajectories from filamentous cells from Fig. 5c in the presence of LatA with trajectories in whole cell (n = 7200), mother compartment (n = 4200) and filament compartment analyzed (n = 2920). Medians and interquartile ranges are indicated with **** < 0.0001 and ** < 0.01. **C**) The actin cytoskeleton restricts GEM diffusion in budding cells. Left panel: effective diffusion of all trajectories from budding cells in the absence (DMSO) or the presence of LatA. Cells from Fig. 5b, with 5800-7200 trajectories for each condition. Medians and interquartile ranges are indicated; **** < 0.0001. Right panel: effective diffusion of all trajectories from filamentous cells in the absence of (DMSO) or presence of LatA. Cells from Fig. 5c, with 7200-7440 trajectories for each condition. Medians and interquartile ranges are indicated; ** < 0.01.

https://doi.org/10.1038/s41564-025-02205-2

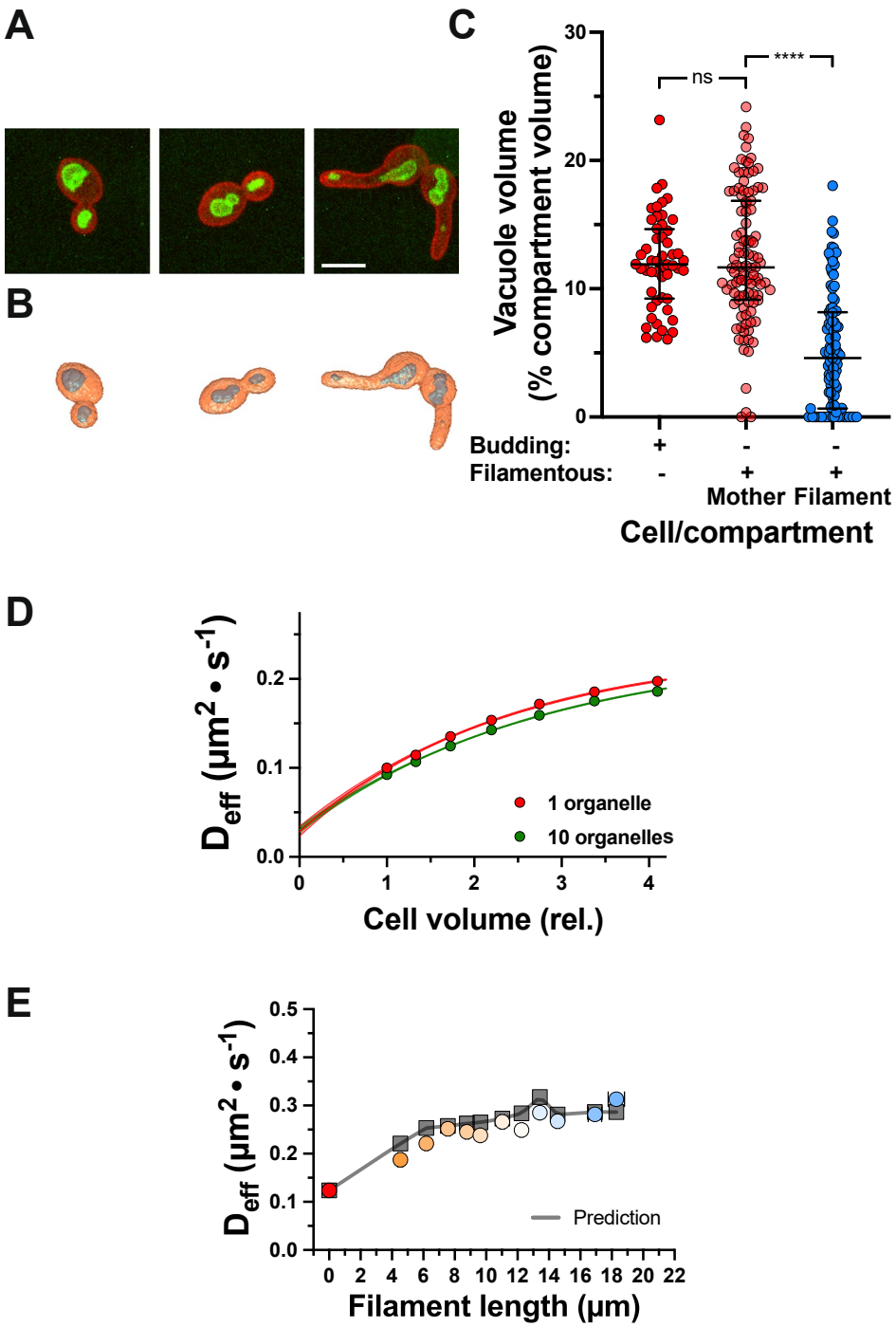

Extended Data Fig. 3 | The vacuole is found predominantly in the mother cell compartment in filamentous cells, simulations with inaccessible organelles and predictive equation taking into account inaccessbile volume. A) Images of vacuoles in representative budding and filamentous cells. A strain in which the vacuoles were visualized using an Mlt1-GFP fusion (vacuole membrane ABC transporter) that also expressed plasma membrane targetted RFP (strain PY7532) was imaged and maximum projections of 20 ×0.2 µm z-section are shown (two independent experiments). **B**) Surface rendered images of plasma membrane and vacuole. A tailor-made Matlab program was used to segment and generate 3-dimensional surface rendered images (plasma membrane in orange and vacuole in grey). **C**) Vacuole volume is reduced in filament compared to mother cell compartment. Volumes of vacuole and cell/compartment were determined from segmented images acquired as in S3A using a tailor-made Matlab program. Medians (n = 52 or 103 cells from two independent experiments) and interquartile ranges are indicated with **** < 0.0001 either using the Mann-Whitney U test for both or the paired two-sided t-test for the mother-filament comparison and ns not significant. **D**) Simulation of GEM diffusion upon cell volume increase is not dramatically affected by number of organelles. Particle D_{eff} in a cylindrical, with ribosome crowders 20% at initial cell volume and accessible cytosolic volume of 20%, with either 1 (red circle) or 10 organelles (green circle). Values are D_{eff} means (6000 particle simulations) carried out 10 times. Data fit with an exponential plateau equation, $r^2 > 0.99$, 95% confidence levels shown. **E**) Theoretical equation for diffusion yields a good fit to the experimental data. Symbols (circles, red to blue color indicating filament length) are data (filament length bins) from Fig. 1d and grey squares/predicted line are from theoretical equation (Eq. 2), using GEM accessible volumes from the results in Fig. 2e. Correlation coefficient, $r^2 = 0.83$.

https://doi.org/10.1038/s41564-025-02205-2

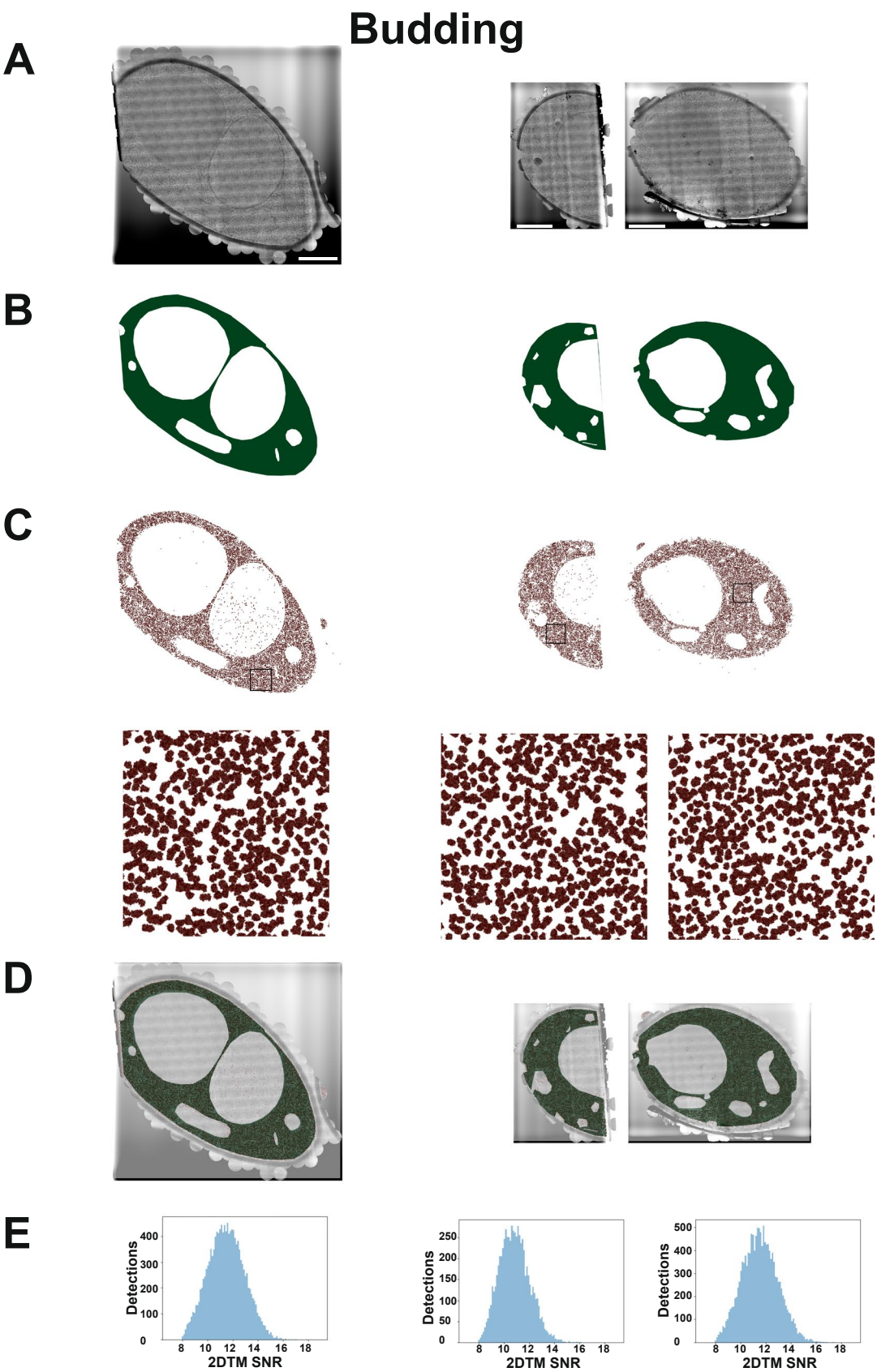

Extended Data Fig. 4 | 2D Template matching of 60S ribosomal subunits in cryo-EM images of budding cells. A) Montage of cryo-EM exposures of three representative cells. Bar is 1 µm. **B**) Manual segmentation of cytosolic regions. **C**) 2DTM detections of the 60S ribosomal subunit, with regions of insets indicated by black square and insets shown (below). **D**) Overlays of **A-C**. **E**) Histogram of 2DTM SNR of 60S ribosomal subunit detections.

https://doi.org/10.1038/s41564-025-02205-2

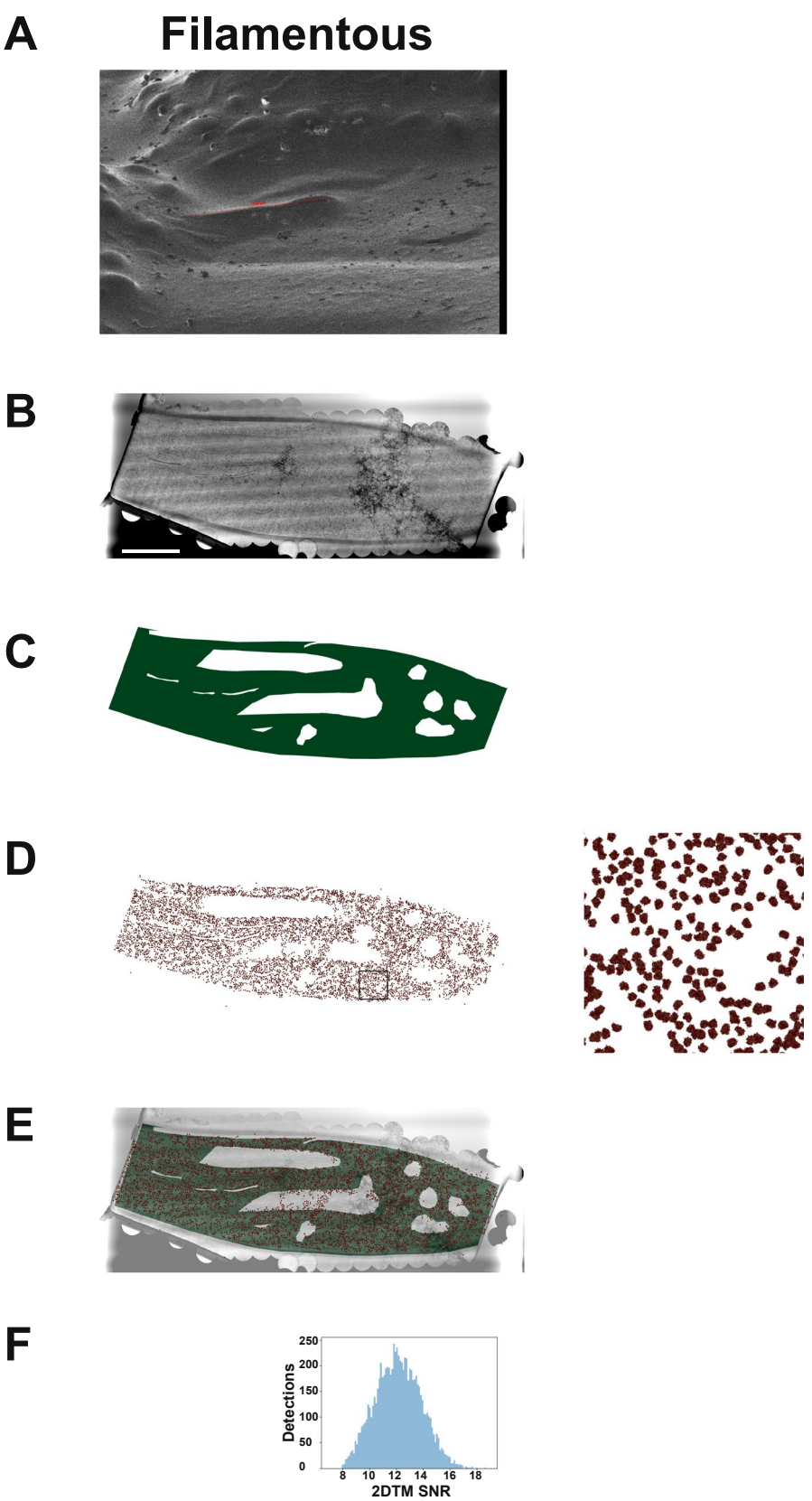

Extended Data Fig. 5 | 2D Template matching of 60S ribosomal subunits in cryo-EM images of filamentous cells. A) Images of a representative cell taken by the focused ion beam prior to milling. Length of filaments was measured using the image viewer of the AutoTEM software. **B**) Montage of cryo-EM exposures of representative cells. Bar is 1 µm. **C**) Manual segmentation of cytosolic regions. **D**) 2DTM detections of the 60S ribosomal subunit with regions of insets indicated by black square and insets shown (right). **E**) Overlays of **B**-**D**. **F**) Histogram of 2DTM SNR of 60S ribosomal subunit detections.

https://doi.org/10.1038/s41564-025-02205-2

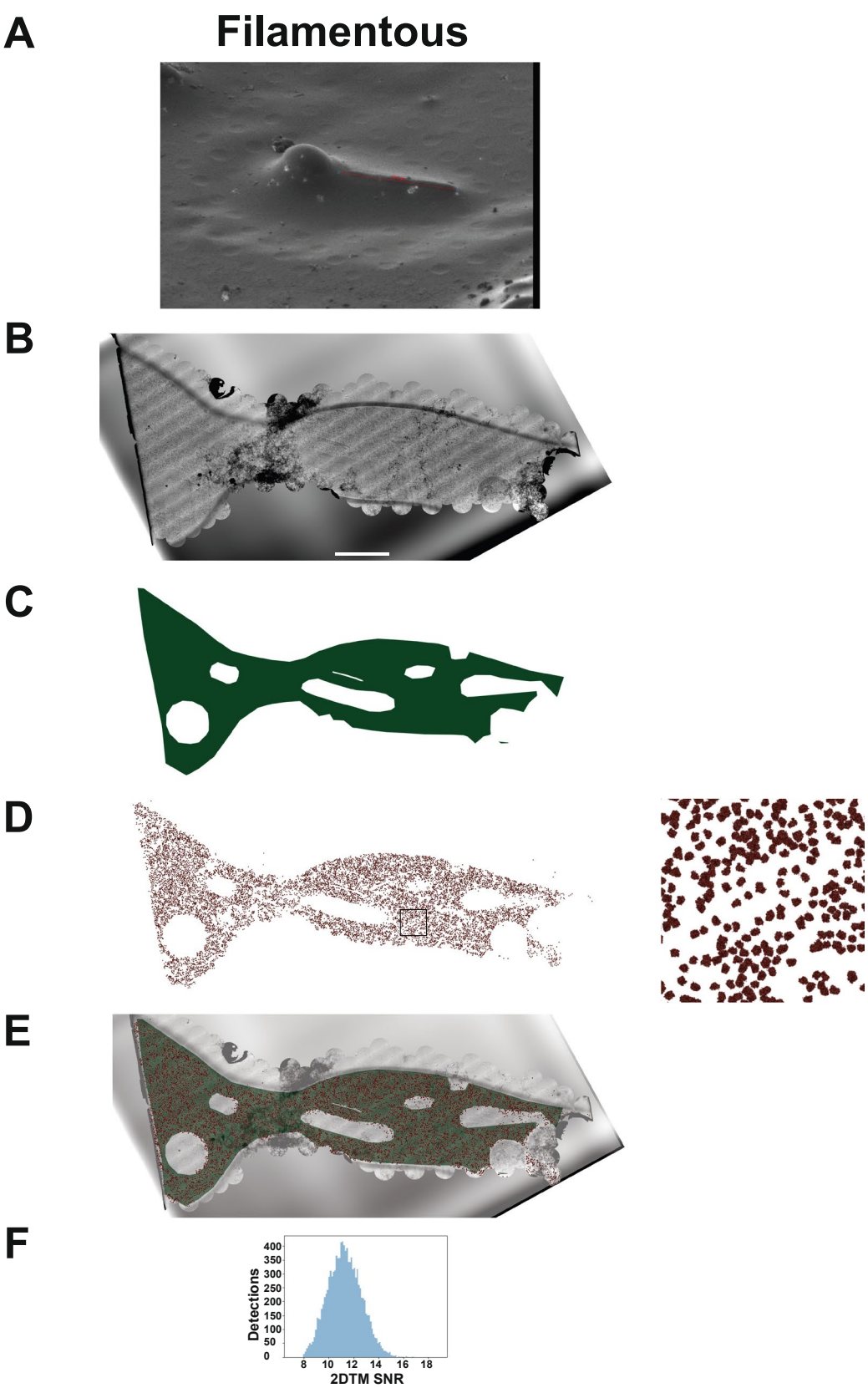

Extended Data Fig. 6 | 2D Template matching of 60S ribosomal subunits in cryo-EM images of filamentous cells. A) Images of a representative cell taken by the focused ion beam prior to milling. Length of filaments was measured using the image viewer of the AutoTEM software. **B**) Montage of cryo-EM exposures of representative cells. Bar is 1 µm. **C**) Manual segmentation of cytosolic regions. **D**) 2DTM detections of the 60S ribosomal subunit with regions of insets indicated by black square and insets shown (right). **E**) Overlays of **B**-**D**. **F**) Histogram of 2DTM SNR of 60S ribosomal subunit detections.

https://doi.org/10.1038/s41564-025-02205-2

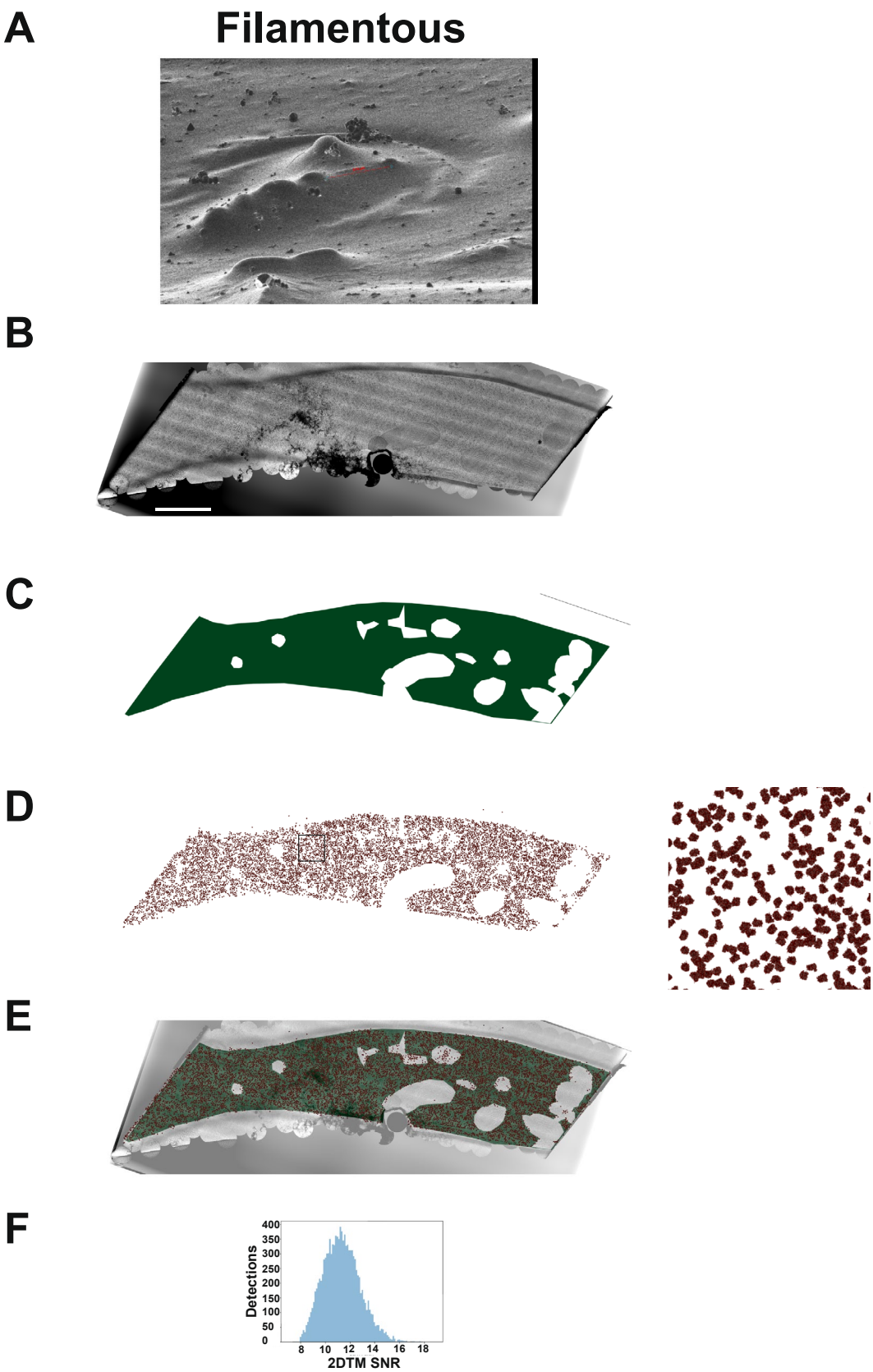

Extended Data Fig. 7 | 2D Template matching of 60S ribosomal subunits in cryo-EM images of filamentous cells. A) Images of a representative cell taken by the focused ion beam prior to milling. Length of filaments was measured using the image viewer of the AutoTEM software. **B**) Montage of cryo-EM exposures of representative cells. Bar is 1 µm. **C**) Manual segmentation of cytosolic regions. **D**) 2DTM detections of the 60S ribosomal subunit with regions of insets indicated by black square and insets shown (right). **E**) Overlays of **B**-**D**. **F**) Histogram of 2DTM SNR of 60S ribosomal subunit detections.

https://doi.org/10.1038/s41564-025-02205-2

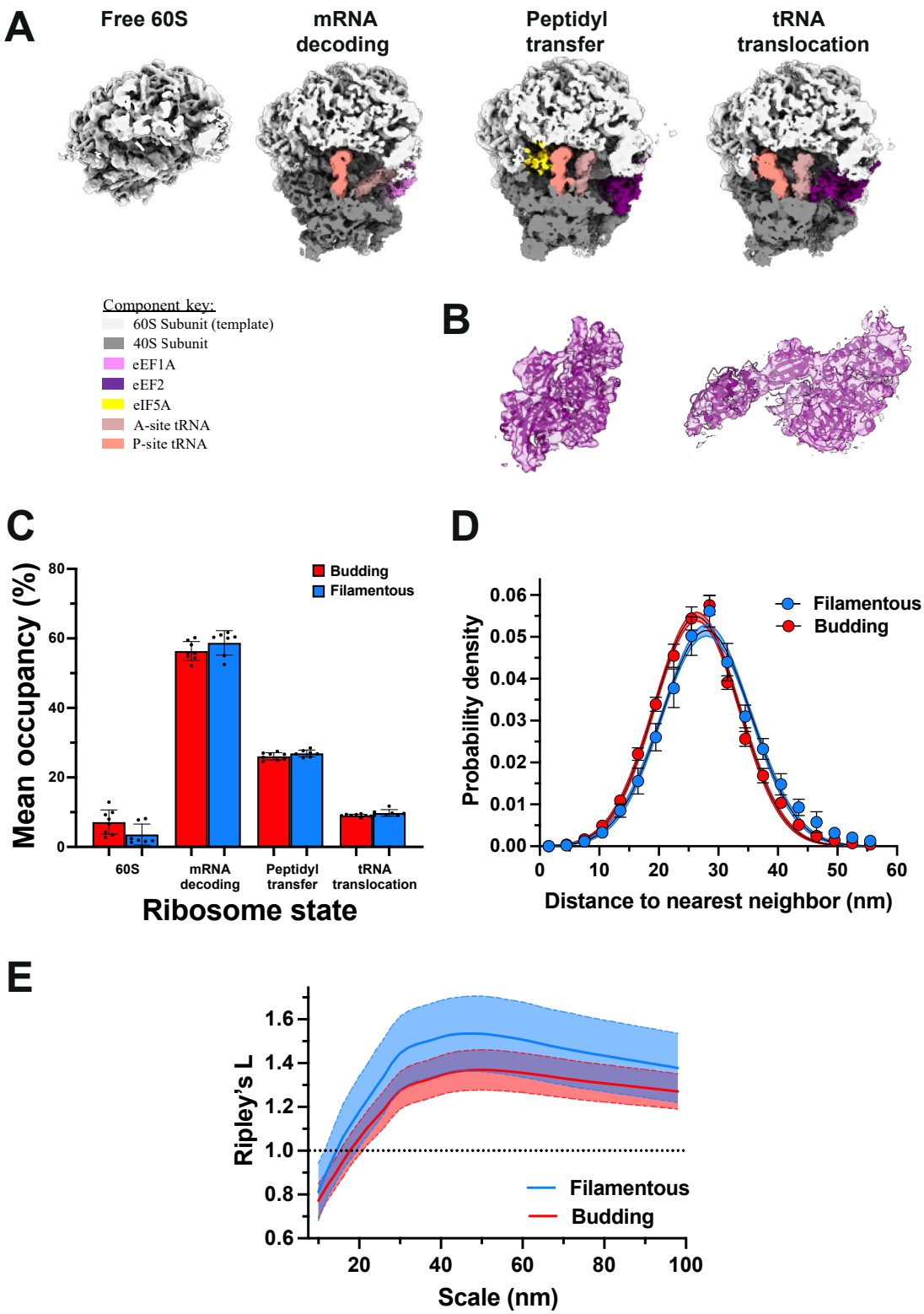

Extended Data Fig. 8 | Ribosome states and clustering in budding and filamentous cells are similar. A) Ribosome compositional and conformational heterogeneity determined by *in-situ* cryo-EM. Distinct classes corresponding to different stages of translation elongation display compositional heterogeneity. Color key for all displayed components displayed. **B**) One example of conformational heterogeneity, eEF2 in different conformations, extended and compact, similar to that previously detailed[68]. **C**) Percentage of different states of translation elongation in budding and filamentous cells. Mean and SD occupancy determined from 7 and 8 budding and filamentous cells. Differences between budding and filamentous cells were not statistically significant. **D**)-**E**) First and second order point pattern analysis of ribosomes in budding and filamentous cells. **D**) Nearest neighbor analysis of ribosome distribution. Mean probability density with SD shown ($n = 7$ and 8 cells). Data fit with an gaussian equation, $r^2 > 0.95$, 95% confidence levels shown. **E**) Ripley's L function second order point pattern analysis of ribosome complex distribution in budding and filamentous cells. Values of 1 indicate random distribution and values above 1 indicate clustering at a given scale. Mean values and SD shown.

https://doi.org/10.1038/s41564-025-02205-2

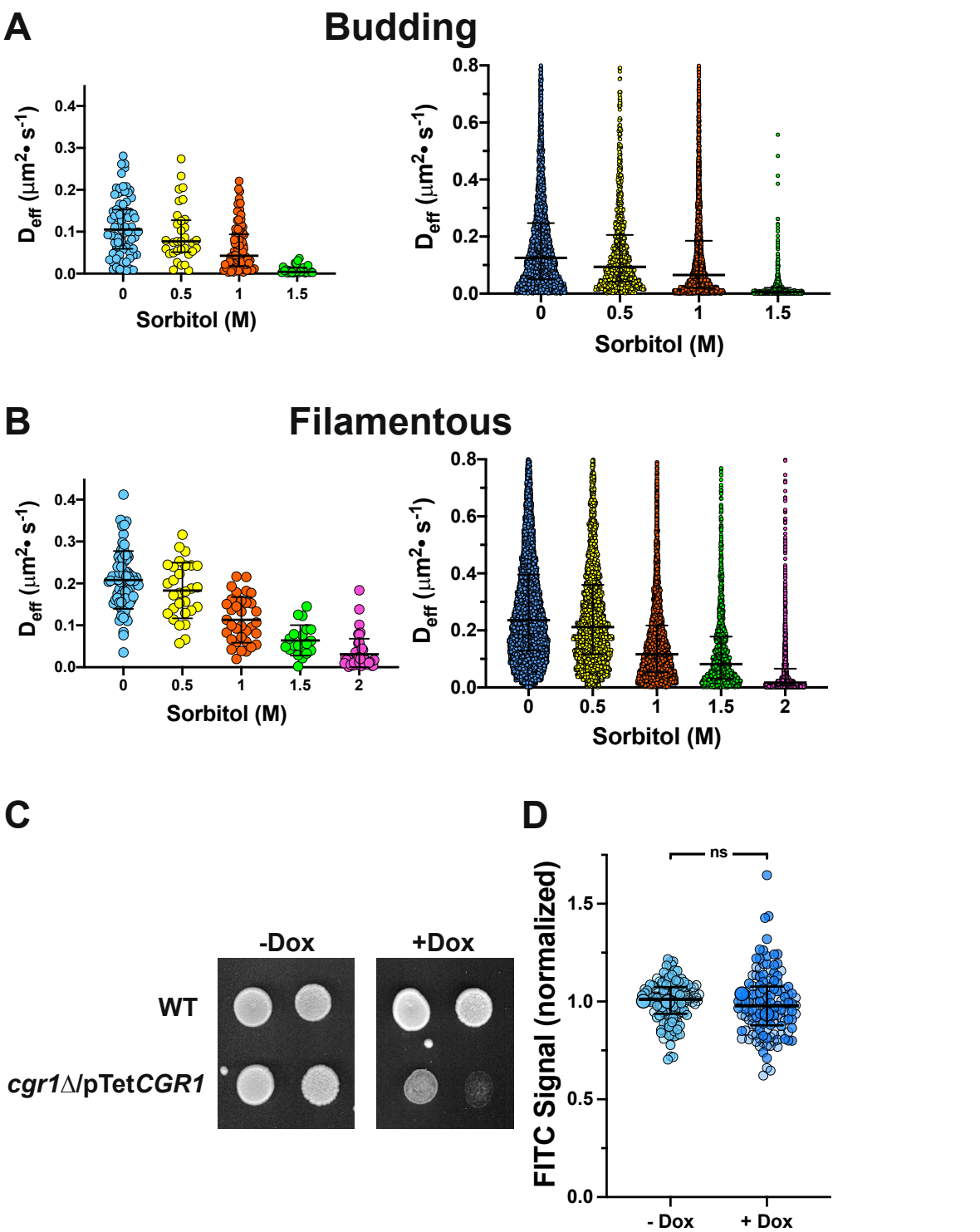

Extended Data Fig. 9 | GEM effective diffusion is reduced with increasing sorbitol concentrations and repression of *CGR1* results in slow growth. **A**) Increasing sorbitol concentration decreases GEM effective diffusion in budding cells. Median D_{eff} of cells (n = 26-95 cells from 4 independent experiments) from Fig. 5a, with 11 - 200 trajectories per cell (left), and effective diffusion of all trajectories from budding cells in Fig. 5a, with 600-4000 trajectories (right), as a function of sorbitol concentration. Medians and interquartile ranges are indicated. **B**) A higher concentration of sorbitol is required to fully abolish GEM dynamics in filamentous cells, compared to budding cells. Median D_{eff} of cells (n = 20-71 cells from 4 independent experiments) from Fig. 5a with 11 - 200 trajectories per cell (left), and effective diffusion of all trajectories from filamentous cells from Fig. 5a, with 600-4000 trajectories (right), as a function of sorbitol concentration. Medians and interquartile ranges are indicated. **C**) Indicated strains were incubated with or without 5 μg/ml Dox on rich media containing agar for 2 days. **D**) Total protein levels are not affected upon repression of *CGR1*. FITC was used to label total proteins in cells grown in the presence and absence of Dox (n = 65-70 cells per experiment, total of 135 cells from two independent experiments; small symbols mean signal of individual cells and large symbol medians of each experiment with interquartile range shown) normalized to median budding signal for each experiment, with ns not significant. Images were acquired and signals (protein concentration) quantitated as described in Fig. 4c.

nature microbiology

Supplementary information

https://doi.org/10.1038/s41564-025-02205-2

Decreased cytoplasmic crowding via inhibition of ribosome biogenesis can trigger *Candida albicans* filamentous growth

In the format provided by the authors and unedited

Supplementary Table 1a. Strains used in this study.

Strain number	**Relevant Genotype**	**Source**
BWP17	*ura3Δ::λimm434/ura3Δ::λimm434 his1Δ::hisG/his1Δ::his arg4::hisG/arg4Δ::hisG*	1
PY173	Same as BWP17 with *ENO1/eno1::ENO1-tetR ScHAP4AD-3xHA-ADE2*	2
PY6413	Same as BWP17 with *adh1Δ::ADH1p-Pfv-GFPγ^{G206K}-ARG4*	This study
PY6414	Same as BWP17 with *adh1Δ::ADH1p-Pfv-GFPγ^{G206K}-CdHIS1*	This study
PY6523	Same as PY6413 with *tef1Δ::TEF1p-LifeAct-mScarlet-HIS1*	This study
PY6599	Same as BWP17 with *tef1Δ::TEF1p-Pfv-GFPγ^{G206K}-CdHIS1*	This study
PY7287	Same as PY173 with *CGR1*/*cgr1*Δ::*CdHIS1*	This study
PY7301	Same as PY7287 with *cgr1::URA3pTet$_{off}$CGR1*	This study
PY7322	Same as PY7301 with *adh1Δ::ADH1p-Pfv-GFPγ^{G206K}-ARG4*	This study
PY7398	Same as BWP17 with *adh1Δ::ADH1p-GFPγ^{G206K}-ARG4*	This study
PY7526	Same as PY7322 with *HWP1Δ::HWP1p-mScarlet-SAT1*	This study
PY7532	Same as BWP17 with *RP10::ARG4- pACT1-mScarlet-Ct$_{Rac1}$, MLT1::MLT1-GFPγ-URA3*	This study
PY7547	Same as BWP17 with *adh1Δ::ADH1p-GFPγ-LoxP-ARG4-LoxP*	This study

Supplementary Table 1b. Oligonucleotides used in this study.

Primer	Sequence (5' → 3')
ADH1p-PfVp	CCAGAATTATTTTTTTTTCATCAGTTTAACAACAACAAACGTTATTGT CATACAACAACAACAACAAATACAAAAACAATTATGttatcaattaatccaac
CaGFPγpA206K-BamHI	ccagacaaccattacttatccactcaatctAAAttatccaaGgatccaaacgaaaagagagaccac
CaGFPγmA206K-BamHI	gtggtctctcttttcgtttggatcCttggataaTTTagattgagtggataagtaatggttgtctgg
CaADH1KIxFP_S1	ccagaattatttttttttcatcagtttaacaacaacaaacgttattgtcatacaacaacaacaacaaatacaaaaacaatt atgGGTGCTGGCGCAGGTGCT
CaADH1KIxFP_S2	ctgggtaatccttgtagactaattgaccaccattggtatcaaagacaacggctttttgagttttgggatttgttcagaca tTCTGATATCATCGATGAATTCGAG
CaHWP1promKIxFP_S1	tttccattcaacttgttttctcaacaatatcaaacacaacaggaatctcctatagtcactcgcttttagtttcgtcaatatg GGTGCTGGCGCAGGTGCTTC
CaHWP1promKIxFP_S2	cgaaaattgaaaaacaatcaaaattagaaaaaaaagaaatcccaaaaaaagaacaaaacttagtatcagttattaga attaTCTGATATCATCGATGAATTCGAG
NotITef1pLifeActS1	gcgcggccgccgtcatcttgatttttacttcttcttcttcttcttttccttttcttcacacattatagtcataatcaatcAT GGGTGTCGCAGATTTGATCAAGAAATTCGAAAGCATCTCAAAGGAAG AAggtgctggcgcaggtgct
CamScarletmAscI	cggcgcgccTTTATATAATTCATCCATACCACC
CaMLT1XFP_S1	gttgcagaattcgattcacctcaaaacttgttgaagaacaaagacagtattttctactctcttgccaaagaaggtggat acatagatGGTGCTGGCGCAGGTGCTTC
CaMLT1XFP_S2	gcatttaaatagttgaaaaagaaatgtaaactaaaaaaaatattattgtataaataaaaaaatcactatatgaatatatat cgcaccgatatataTCTGATATCATCGATGAATTCGAG
CGR1.P1	CAATACGAAGAAATACCC
CGR1.P2	GCATGCATTTTAGTAGCC
ACT1.P1	ATGTTCCCAGGTATTGCTGA
ACT1.P2	ACATTTGTGGTGAACAATGG
ECE1.P1	CCAGAAATTGTTGCTCGTGTTG
ECE1.P2	CAGGACGCCATCAAAAACG

HGC1.P1	AAAGCTGTGATTAAATCGGTTTTGA
HGC1.P2	AATTGAGGACCTTTTGAATGGAAA
HWP1.P1	CGGAATCTAGTGCTGTCGTCTCT
HWP1.P2	TAGGAGCGACACTTGAGTAATTGG

References

1. Wilson, R. B., Davis, D. & Mitchell, A. P. Rapid hypothesis testing with *Candida albicans* through gene disruption with short homology regions. *J. Bacteriol.* **181**, 1868–1874 (1999).

2. Vernay, A., Schaub, S., Guillas, I., Bassilana, M. & Arkowitz, R. A. A steep phosphoinositide bis-phosphate gradient forms during fungal filamentous growth. *J. Cell Biol.* **198**, 711–730 (2012).